Behavior of Amagmatic Orogenic Geothermal Systems: Insights From the Agua Blanca Fault, Baja California, Mexico

Daniel Carbajal-Martínez[1] [ID], **Christoph Wanner[1]** [ID], **Larryn W. Diamond[1]**, **Loïc Peiffer[2,3]**,
John M. Fletcher[2] [ID], **Claudio Inguaggiato[2]** [ID], and **Manuel Contreras-López[4]** [ID]

[1]Rock–Water Interaction Group, Institute of Geological Sciences, University of Bern, Bern, Switzerland, [2]Departamento de Geología, Centro de Investigación Científica y de Educación Superior de Ensenada (CICESE), Ensenada, México, [3]Unidad La Paz (ULP), Centro de Investigación Científica y Educación Superior de Ensenada (CICESE), La Paz, México, [4]Laboratorio Universitario de Geoquímica Isotópica (LUGIS), Instituto de Geofísica, Universidad Nacional Autónoma de México (UNAM), Ciudad de México, México

Abstract Amagmatic geothermal systems within regional-scale orogenic faults are promising renewable resources for heat and possibly electricity production. However, their behavior needs to be better understood to improve their exploration and assessment of energy potential. To provide more insight, we report geochemical, geological, and geophysical studies from seven hot spring sites strung along a 90 km segment of the Agua Blanca Fault, which traverses a mountainous region of northern Baja California, Mexico. Our results show that topographic heads drive infiltration of meteoric water deep into basement rocks, where it is heated according to the local geothermal gradients. Long paths lead to long water residence times and high ^{3}He/He$_{total}$ fractions. The hot water ascends along preferentially permeable zones within the ABF, discharging at temperatures from 37°C in inland springs to 102°C on the Pacific coast. Higher discharge temperatures correlate positively with the degree of extensional fault displacement (a proxy for fault permeability). Correlations between hydraulic head gradients, residence times, and ^{3}He/He$_{total}$ of the thermal waters show that the hydraulic head gradient controls the length and depth of the flow paths, whereas the magnitudes and locations of the discharge sites are controlled by fault permeability. Optimal conditions at the coast allow the 120°C temperature threshold for electricity production to be reached at relatively shallow depths (<2 km), demonstrating the potential of orogenic geothermal systems not only for exploitation of hot discharging water but also for EGS exploitation of the hot rocks that surround the water upflow zones.

Plain Language Summary The deep circulation of meteoric water in areas not affected by volcanic heat represents underexplored renewable energy sources for heat or electricity production. A challenge for exploration is that the processes and forces that drive the hot water circulation in such systems are not fully understood. To obtain new insights, we undertook a geochemical, geological, and geophysical study of seven hot spring sites strung along a 90 km long fault zone across the northern Baja California Peninsula in Mexico. Our data show that rainwater infiltrates deep into mountainous areas and modifies its chemical composition and temperature in the absence of any magmatic heat source. We also discovered that the local permeability of the fault zones controls the discharge temperature of the hot springs and, thus, the amount of thermal energy that could be potentially exploited from such systems. Other relevant system parameters, such as the depth of water infiltration and the subsurface water residence time, are controlled by the differences in water pressure under high and low points in the topography and by the distance between the point of infiltration of rainwater and its subsequent discharge location.

1. Introduction

Regional-scale faults in mountainous orogens often host hot springs with potential as geothermal resources, even in areas where magmatic heat is absent and heat fluxes are moderate (Wanner et al., 2019). The springs are the discharge sites of meteoric water that has infiltrated at high altitudes, circulated deep through the orogen along fracture networks and faults where it has acquired heat from the wall rocks, and then ascended through preferentially permeable upflow zones to low points in the topography (Alt-Epping et al., 2022; López & Smith, 1996; Menzies et al., 2016; Stober et al., 2022). The meteoric water circulation through the purely brittle realm of the crust is driven by high hydraulic heads and induced by the high relief of the topography. Penetration depths of

Investigation: Daniel Carbajal-Martínez, Christoph Wanner, Larryn W. Diamond, Loïc Peiffer, John M. Fletcher, Claudio Inguaggiato, Manuel Contreras-López

Methodology: Daniel Carbajal-Martínez, Larryn W. Diamond, Loïc Peiffer, John M. Fletcher, Manuel Contreras-López

Project administration: Loïc Peiffer

Resources: Christoph Wanner, Larryn W. Diamond, Loïc Peiffer, John M. Fletcher, Claudio Inguaggiato, Manuel Contreras-López

Software: Daniel Carbajal-Martínez, John M. Fletcher, Claudio Inguaggiato

Supervision: Christoph Wanner, Larryn W. Diamond, Loïc Peiffer

Validation: Larryn W. Diamond, Loïc Peiffer, John M. Fletcher

Visualization: Daniel Carbajal-Martínez, Larryn W. Diamond, Loïc Peiffer, John M. Fletcher, Manuel Contreras-López

Writing – original draft: Daniel Carbajal-Martínez

Writing – review & editing: Daniel Carbajal-Martínez, Christoph Wanner, Larryn W. Diamond, Loïc Peiffer, John M. Fletcher, Claudio Inguaggiato, Manuel Contreras-López

meteoric water are deduced to be as high as 9–10 km (Diamond et al., 2018), and in some cases, meteoric water may penetrate the transiently ductile deformation realm (for which additional driving forces are required; McCaig, 1988; Menzies et al., 2014; Upton et al., 1995).

Worldwide occurrences of such amagmatic orogenic geothermal systems include those in the Canadian Rocky Mountains (Grasby & Hutcheon, 2001), Lérida province in the Pyrenees in Spain (Asta et al., 2010), Da Qaidam in China (Stober et al., 2016), Brigerbad in Switzerland (Sonney & Vuataz, 2008), the Eastern Pyrenees in France (Taillefer et al., 2018), Huangshadong in China (Tian et al., 2023), along the Alpine Fault in New Zealand (Coussens et al., 2018; Sutherland et al., 2017), along the Lishan Fault in Taiwan (Chen, 1985; Upton et al., 2011) and the Nepalese Himalaya (Whipp & Ehlers, 2007). These fault-hosted, topography-driven systems are characterized by regional crustal geothermal gradients typically between 20 and 30°C km^{-1} (with exceptionally higher gradients in the Alpine Fault, New Zealand; Sutherland et al., 2017), by temperatures of 100 to at least 250°C at the greatest depths of water circulation, and by spring temperatures of 25–102°C.

Prolonged heat extraction from the wall rocks by water moving along the base of the circulation loop and its redeposition into the wall rocks of the upflow path can create large, three-dimensional, plume-like thermal anomalies of hot dry rock beneath the discharge sites (Wanner et al., 2019). At depths within the reach of drilling (e.g., 2 km), the temperatures in these plumes can exceed the 120°C threshold for electricity generation. Thus, although discharge rates are normally modest, the plumes of hot rock below the springs can be viewed as targets for EGS ("petrothermal") exploitation, which requires artificial hydraulic stimulation to facilitate heat extraction (Wanner et al., 2019).

To improve exploration strategies for this geothermal play, a better understanding is required of how they behave, particularly the controls on their locations and magnitudes. We have therefore undertaken a geochemical, geophysical and geological study of orogenic geothermal systems along the Agua Blanca Fault (ABF) in Ensenada, Baja California, Mexico. We chose this topographically rugged area because it exhibits three favorable features: (a) seven geothermal systems are strung out along a ~90 km stretch of the fault, permitting the quantitative correlation of hydraulic head gradients with the physicochemical properties of the springs; (b) water discharge temperatures vary along the fault from 37 to 102°C, the latter being worldwide the hottest and therefore most prospective amagmatic system to our knowledge; (c) the host fault is active and the rates and magnitudes of tectonic extension along its segments have been quantified (Gold et al., 2020; Wetmore et al., 2019), allowing qualitative assessment of permeability variations along the fault.

In this paper, we take advantage of these features to explore how the interplay of variable fault permeability and hydraulic head gradients control the location and discharge temperatures of the springs. To enable this treatment, we present new analyses of spring compositions, including major solutes, pH, temperature, dissolved gases, O–H stable isotopes, and He–Ne radiogenic isotopes. We calculate water residence times and reservoir temperatures and interpret earthquake hypocenters to estimate depths to the brittle–ductile transition zone (BDTZ) and geothermal gradients. Finally, we identify recharge zones from O–H stable isotopes and topographic maps, calculate hydraulic head gradients, and integrate our collective results with structural data from the literature to construct a conceptual model of the behavior of geothermal systems along the ABF. As well as providing new insight into the hydraulic controls on the geothermal systems, our new data and correlations will serve as calibration targets for future 3D numerical simulations of water circulation through the ABF, from which additional parameters can be quantified and conclusions drawn for exploration strategies.

1.1. Geology and Geothermal Manifestations of the Study Area

The study area is located in the northwest of the Baja California Peninsula, Mexico (Figure 1a) and encompasses the northwestern sector of the geological province known as the Peninsular Ranges Batholith. The rocks in this province (Figure 1b) can be divided into three tectonostratigraphic groups (Gastil et al., 1975): (a) Pre-batholithic rocks consisting of a Triassic–Jurassic belt of metamorphosed quartz-bearing sandstone, argillite, and minor carbonate rocks located in the eastern part of the study area. Part of the same group is the Alisitos Formation, a Lower Cretaceous belt of volcanic (andesite to dacite) and volcaniclastic (tuff and pyroclastic) rocks interbedded with sedimentary mudstone, sandstone, and limestone along the western flank of Baja California; (b) Batholithic rocks of Cretaceous age dominated by tonalite (73 vol.%), granodiorite (23 vol.%), with minor gabbro and diorite (2 vol.%), and quartz monzonite (2 vol.%). These underlie the entire study area, having been emplaced successively from west to east between 140 and 80 Ma (Gastil et al., 1975; Ortega-Rivera, 2003); (c) Post-batholithic
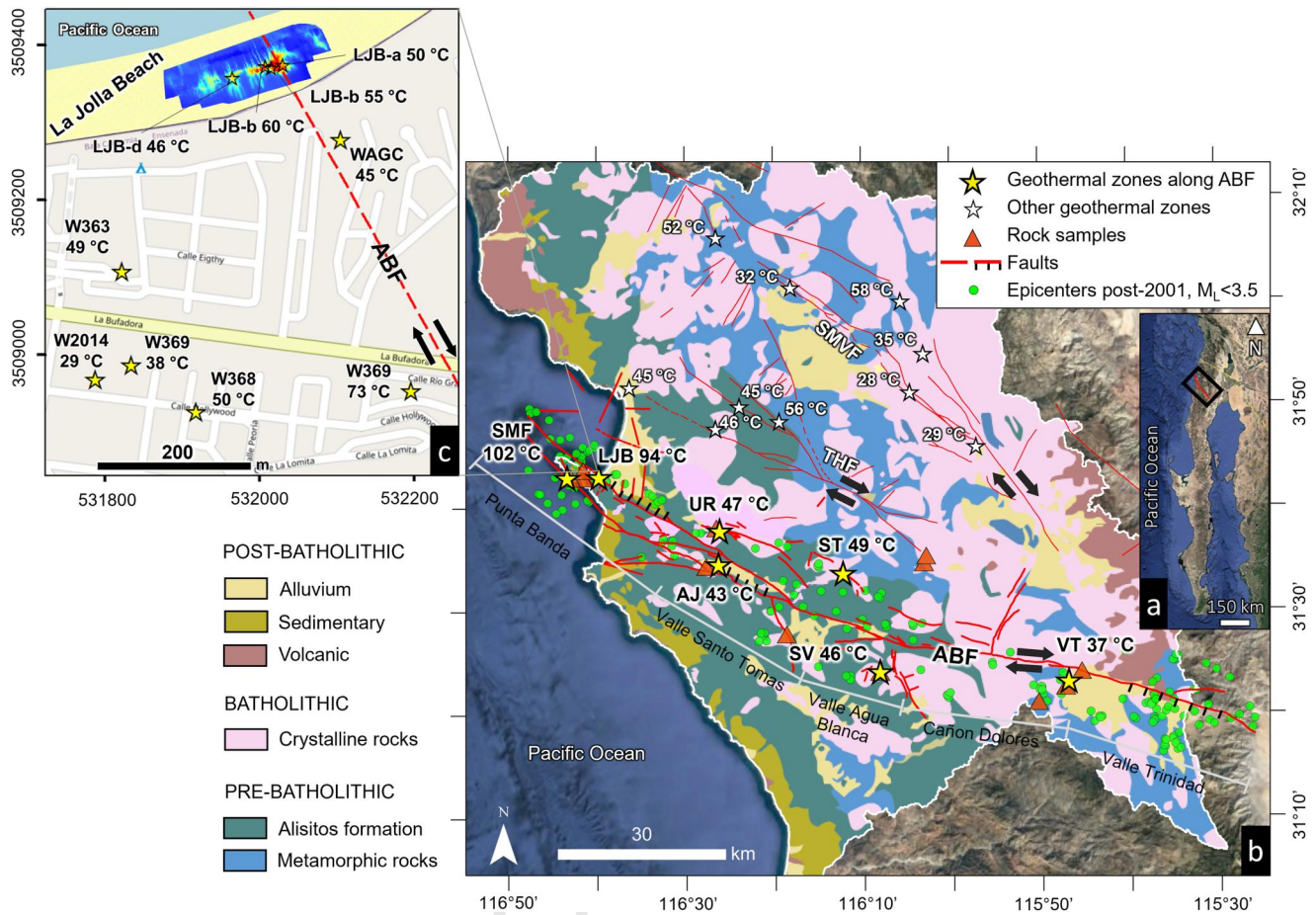
Figure 1. Location of the study area and its geological and geothermal features. (a) Location in Baja California, Mexico (black rectangle). (b) Geological map modified from Gastil et al. (1975) with locations of 17 orogenic amagmatic geothermal systems (stars) along fault traces (red lines). Yellow stars mark the thermal waters reported in this study. To facilitate the discussion, these are divided into five geographic zones labeled Punta Banda in the northwest to Valle Trinidad in the southeast. (c) Detailed location of La Jolla Beach thermal anomaly (Carbajal-Martínez et al., 2020) and its surrounding domestic thermal wells (UTM 11N coordinates).

rocks comprising the Late Cretaceous Rosario Group of marine mudstones, sandstones and granitic conglomerates; Eocene–Paleocene marine mudstones and sandstones; and Miocene volcanic rocks (rhyolite, andesite, and basalt).

The study area is an active tectonic zone encompassing three steeply dipping dextral fault systems: Agua Blanca Fault (ABF), Tres Hermanos Fault (THF), and San Miguel-Vallecitos Fault (SMVF) (Figure 1b). These collectively host a total of 17 geothermal systems, manifested by hot springs, submarine fumaroles, domestic thermal wells, and coastal thermal anomalies (Figures 1b and 1c). Chemical and isotopic analyses of water and gas discharges from some of these geothermal systems have confirmed their meteoric origin and have revealed no evidence of a magmatic heat source. This observation aligns with the absence of post-Miocene magmatic rocks in the area (Arango-Galván et al., 2011; Barry et al., 2020; Beltrán-Abaunza & Quintanilla-Montoya, 2001; Gastil & Bertine, 1986; Polyak et al., 1991; Vidal et al., 1981).

The present study focuses on amagmatic geothermal systems occurring along the active ABF (Figure 2a). This subvertical, west–northwest-trending (276–302°) dextral–normal fault first became active between 3.3 and 1.5 Ma (Wetmore et al., 2019). It is transtensional along its ~150 km exposed length (downthrown to the north in the NW and to the south in the SE) and traverses nearly the entire Baja California Peninsula, extending beneath the Pacific Ocean in the northwest (Figure 2a). The ABF has several branches recognizable from geomorphological features such as triangular facets, deviated streams, vegetation lines, and uplifted marine terraces (Allen et al., 1960; Rockwell et al., 1989). Although seismic events with magnitudes up to 3 are relatively infrequent
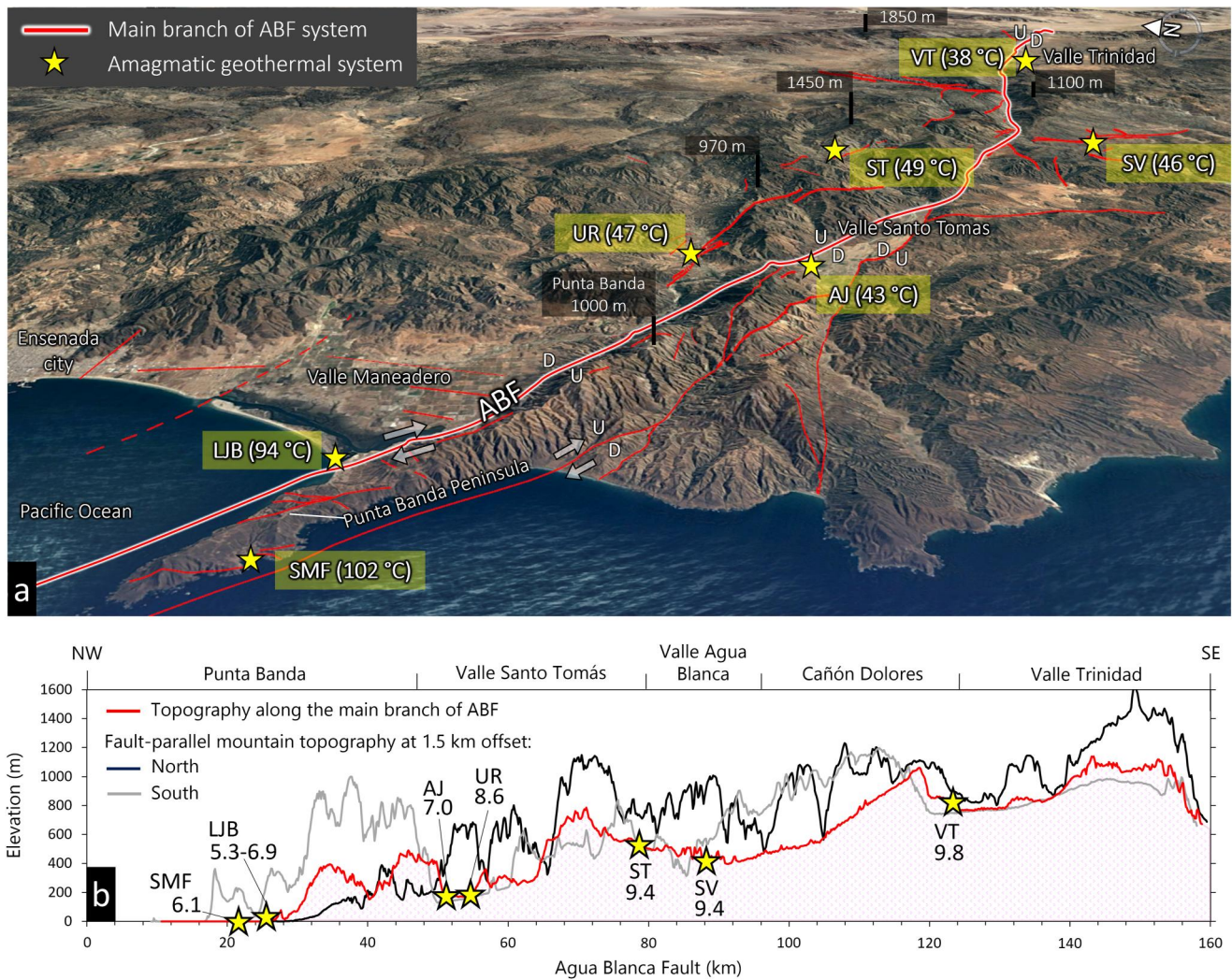
Figure 2. Oblique aerial view and topographic profile of the study area. (a) 3D view highlighting the rugged topography, the location of amagmatic geothermal systems linked to the dextral Agua Blanca Fault (ABF), and the discharge temperatures of thermal springs. As an indication of scale, the distance between the two fault branches on either side of the Punta Banda Peninsula is approximately 4 km, and the Valle Trinidad spring (VT) lies 135 km from La Jolla Beach (LJB). The fault exhibits both dip-slip movement upwards (U) and downwards (D). (b) Topographic elevation profiles displaying the main trace of the ABF (in red) as well as two additional profiles (in black and gray) that run 1.5 km parallel to the north and south of the main trace of the fault. The vertical axis exaggerated ~20 times. Numbers beside spring names show the pH values of the thermal waters.

compared to the San Miguel-Vallecitos Fault (Figure 1b), earthquakes with magnitudes of 6–7 occur at a recurring interval of 75–200 years in the central zone of the ABF (Ortega-Rivera et al., 2018).

Thermal water discharge in five valleys intersected by faults belonging to the ABF system. From southeast to northwest, these are Valle Trinidad, Cañon Dolores, Valle Agua Blanca, Valle Santo Tomas, and the coastal plains flanking the Punta Banda Peninsula (Figure 2b). Geologic and geodetic studies in these valleys indicate consistent slip rates of 2–4 mm year^{-1} over ~10 Kyr time scales (Gold et al., 2020; Wetmore et al., 2019). However, these valleys exhibit different amounts of strike-slip along different sections. In Valle Trinidad, Cañon Dolores, and Valle Agua Blanca, the fault exhibits its maximum strike-slip of up to 10–12 km. Conversely, in the northwest section, comprising Valle Santo Tomas and Punta Banda, only 5–7 km of strike-slip has occurred. It is important to note that the two northwest zones have undergone higher total dip-slip displacement than elsewhere, with values of 1.16 and 1.25 km (north side down), respectively (Wetmore et al., 2019). Geodetic block modeling, along with previous geological assessments of slip direction, have revealed an increased occurrence of fault-perpendicular extension toward the southeast (3%–10%) and northwest (5%–15%), with lower values observed throughout the central part of the fault (<2%) (Wetmore et al., 2019). Notably, the zone of the ABF with the

highest extension coincides with the location of the hottest thermal waters along the coast of the Punta Banda Peninsula, specifically at La Jolla beach (LJB, 94°C) and at a submarine fumarole (SMF, 102°C) (Carbajal-Martínez et al., 2020; Vidal et al., 1981).

The topography of the study area is characterized by high relief (Figure 2a), which provides the potential energy to drive meteoric water deep into the ABF (e.g., Tóth, 1962, 2009). The main trace of the ABF intersects both ridges and valleys, reaching a maximum elevation of 1,100 m a.s.l. (Figure 2b). Figure 2b also shows two topographic profiles parallel to the main trace of the ABF, one offset by 1.5 km to the north, the other to the south. These profiles are included to indicate that the elevated northern side of the fault (up to ∼1,600 m a.s.l.) serves as the main recharge catchment for water infiltrating the ABF. The only exception is at the Punta Banda Peninsula, where elevations are higher on the southern side of the ABF (up to ∼1,000 m a.s.l.).

2. Materials and Methods

2.1. Water Sampling and Analysis

Fourteen thermal waters (hot springs, domestic thermal wells, intertidal seeps) located along the ABF were sampled in 2018 and 2019 (Table 1). On-site measurements were made for pH (to within ±0.05 units with an OAKTON 150), temperature (to within ±0.4°C with a HANNA HI 93503 thermocouple), and electrical conductivity (EC, to within ±1% with a Thermo Scientific Orion 105A conductivity meter). Samples were filtered through a 0.45 μm MILLIPORE filter and collected in 50 mL High-Density Polyethylene (HDPE) bottles. Samples for cation analysis were acidified using ultra-pure HNO_3. Alkalinity was determined on-site on filtered water samples by titration with a 0.02 M H_2SO_4 solution using bromocresol green and phenolphthalein as indicators.

Analyses were conducted at the geochemical laboratory of the Istituto Nazionale di Geofisica e Vulcanologia–Palermo (INGV–PA), Italy. Anion concentrations were determined using a Dionex ICS-1100 ion chromatograph and cations by Inductively Coupled Plasma Optical Emission Spectroscopy (ICP-OES) with a Jobin Yvon Ultima 2 spectrometer. Analytical uncertainty is ≤1% for concentrations above 1 meq L^{-1} and ≥5% for lower concentrations. Values of $\delta^{18}O$ and δ^2H were determined by Continuous-Flow Isotope Ratio Mass Spectrometry (CF-IRMS). For $\delta^{18}O$, a Thermo Delta V mass spectrometer was used, while δ^2H values were determined using a Thermo Delta XP mass spectrometer. The isotopic ratios are expressed in δ-notation (‰) relative to Standard Mean Ocean Water (SMOW). Uncertainties are less than ±0.1‰ for $\delta^{18}O$ and ±1‰ for δ^2H.

2.2. Gas Sampling and Analysis

Dissolved gases were sampled in 120 cm^3 glass flasks following the methodology of Capasso and Inguaggiato (1998) and Inguaggiato and Rizzo (2004). The gas phase in equilibrium with the water sample inside the glass flask was analyzed on an Agilent® 7890 gas chromatograph at the INGV–PA to determine N_2, O_2, and CO_2 with an analytical uncertainty of ≤5%. The resulting dissolved gas concentrations are reported in cm^3 STP g^{-1} H_2O (0°C and 100 kPa) as calculated using the Bunsen coefficients (Table 2; Capasso & Inguaggiato, 1998; Hamme & Emerson, 2004; Weiss, 1971).

Helium isotopes (^3He and ^4He), Ar, and ^{20}Ne dissolved in the water samples were analyzed. The gas phase in equilibrium with the water sample inside the glass flask was analyzed using a GVI-Helix® SFT mass spectrometer, yielding raw $^3He/^4He$ isotopic ratios, R_{raw}, to within >3% analytical uncertainty. The R_{raw} ratios were normalized to the atmospheric ratio ($R_a = 1.40 \times 10^{-6}$; Sano & Wakita, 1985) and reported as R_{raw}/R_a values (Table 2). Argon and Ne isotopes were analyzed with Helix MC-GVI and Thermo Scientific Helix MC Plus mass spectrometers, respectively, with analytical uncertainties <3%. The R_{raw}/R_a values were corrected for air contamination (R/R_a) following Hilton (1996):

$$R/R_a = ((R_{raw} \times X) - 1) / (X - 1) \qquad (1)$$

$$X = \left(^4He/^{20}Ne\right)/\left(^4He/^{20}Ne\right)_{air} \times \left(\beta_{Ne}/\beta_{He}\right) \qquad (2)$$

Table 1
Chemical and Isotopic Compositions of Thermal Waters Collected Along the Agua Blanca Fault

Class	Type	Sample	T^a (°C)	T_{Geot} (°C)	pH	TDS (g L^{-1})	Na$^+$	K$^+$	Mg^{2+}	Ca^{2+}	Li	B	Cl$^-$	SO$_4^{2-}$	Br$^-$	HCO$_3^-$	F$^-$	SiO$_2$	δ^{18}O (‰)	δ^{2}H (‰)
Inland	Spring	VT	37	105[b]	9.8	0.51	156	1.9	0.04	2.65	33	1,208	137	66	bdl	90	2.1	53.5	−8.5	−61.0
		SV	46	103[b]	9.4	0.34	100	1.1	0.02	2.7	22	135	100	59	bdl	27	3.3	45.9	−7.6	−47.8
		ST[c]	49	108[b]	9.4	0.37	118	1.5	1.0	7.1	NM	NM	105	49	bdl	38	11.6	41.4	−8.3	−53.0
		UR	47	112[b]	8.6	0.75	225	3.1	0.6	15.2	100	785	266	121	0.8	61	4.5	52.7	−7.4	−49.0
	Well	AJ	43	121[b]	7.0	0.88	192	3.2	24.6	70.7	12	1,909	357	113	1.1	72	1.8	43.3	−7.2	−45.0
Coastal	Wells at La Jolla	W368	50	113[d]	6.9	8.60	2,341	93.6	61.8	766.3	1,126	7,128	4,849	386	15.5	56	bdl	48.0	−5.5	−38.0
		W369	73	132[d]	5.3	8.11	2,289	112.0	8.2	685.1	1,355	9,221	4,714	231	17.3	2.4		68.8	−5.3	−36.0
		W363	30	137[d]	6.5	8.63	2,208	93.6	61.8	766.3	1,149	8,059	4,849	386	bdl	56		74.9	−5.8	−38.0
		W2014	29	128[d]	6.2	8.53	2,294	82.2	97.8	700.4	924	7,572	4,894	312	bdl	90		63.0	−5.8	−39.0
		W367	38	138[d]	6.5	8.52	2,370	100.5	41.6	729.6	1,171	8,332	4,888	264	bdl	49		75.5	−5.9	−38.0
		WAGC	45	147[d]	6.4	9.50	2,659	108.7	53.1	802.1	1,255	8,411	5,442	332	bdl	20		85.8	−5.3	−35.0
	Thermal anomaly La Jolla beach	LJB-a	50	156[d]	6.8	13.63	3,961	145.6	190.0	832.9	1,089	9,004	7,738	614	23.7	46		82.8	−4.3	−31.7
		LJB-b	55	158[d]	6.7	12.99	3,733	140.5	150.2	846.9	1,120	9,711	7,396	557	21.7	61		87.3	−4.1	−30.0
		LJB-c	60	152[d]	6.4	10.86	3,002	122.1	95.8	786.2	1,183	8,049	6,279	420	21.3	46		87.2	−5.2	−34.0
		LJB-d	46	137[d]	6.9	15.96	4,440	161.4	342.6	819.7	743	8,460	9,120	904	33.4	90		53.1	−4.3	−29.0
Submarine	Vent	SMF[c]	102	228[d]	6.1	18.95	5,200	410.0	80.0	1,600.0	3,000	23,000	10,800	351	NM	347	1.8	156	−3.5	−25.4
Seawater	Seawater	SW	19	-	8.1	34.20	10,729	329.9	1,021.3	413.0	165	4,509	18,967	2,610.2	67.4	45	bdl	2.3	−0.6	−3.0

Note. Individual solute concentrations are given in mg L^{-1}; Lithium and boron concentrations are given in µ L^{-1}. T_{Geot} values are temperatures calculated from solute geothermometers. Stable isotope ratios are expressed as δ values (‰) relative to Standard Mean Ocean Water (SMOW). bdl: Data below detection limit; NM: not measured. [a]Measured discharge temperature of spring. [b]Temperature calculated using Na/K geothermometer. [c]Data from Vidal et al. (1981) and Zúñiga (2010). [d]Temperatures calculated using the unmixed SiO$_2$ concentrations (Table S3 in Supporting Information S1) in combination with the quartz geothermometer (Equation 12).

Table 2
Chemical and Isotopic Compositions of Gases Dissolved in Thermal Waters (Sample Type DG, Expressed in cm³ STP g⁻¹ H₂O) and of Bubbling Gases (Type BG, Expressed in Volume %) Along the Agua Blanca Fault

Sample	Type	N_2 (10^{-2})	O_2 (10^{-4})	CO_2 (10^{-3})	^4He (10^{-6})	^{20}Ne (10^{-7})	$^4He_{ex}$ (10^{-6})	$N_2/$ Ar	$^4He/^{20}Ne$	R_{raw}/R_a [a]	$\pm R/R_a$ [b] (10^{-3})	R/R_a [c]	F_m [d] (%)	F_r [e] (%)	Age [f] (Kyr)
VT[g]	DG	1.50	1.37	0.33	4.35	1.68	4.85	28.4	25.9	0.57	6.1	0.56	6.6	93.4	66
SV[g]	DG	2.30	6.39	0.10	4.88	5.75	4.72	13.9	8.5	0.95	9.6	0.94	11.1	88.9	65
UR[g]	DG	1.79	6.61	0.27	6.23	6.34	6.06	9.8	9.8	0.59	8.4	0.58	6.7	93.3	83
AJ[g]	DG	1.65	1.66	17.0	2.10	1.88	2.07	37.8	11.2	0.36	6.6	0.35	4.0	96.0	28
W369	DG	1.00	25.3	4.37	0.81[h]	2.67[h]	0.56	32.1	3.0	0.19	7.1	0.12[h]	1.2	98.8	8
W368	DG	1.30	6.20	13.8	0.56[h]	2.76[h]	0.36	33.8	2.0	0.19	9.1	0.06[h]	0.6	99.4	5
LJB-c	DG	NM	NM	NM	1.70[h]	3.22[h]	1.07		5.2	0.29	4.6	0.26[h]	2.9	97.1	15
SMF[i]	BG	56.1	0.29	1.8	0.08	NM		160		0.54					
ASW[i]		1.23	66.0	0.31	0.045	1.63		38.6	0.28						

Note. NM: not measured. [a]Raw measured ³He/⁴He ratio (R_{raw}) normalized to the ³He/⁴He ratio of air (R_a). [b]Uncertainty in R_{raw}/R_a. [c]³He/⁴He ratio (R) corrected for air contamination and normalized to the ³He/⁴He ratio of air (R_a). [d]Fraction of mantle He (see text). [e]Fraction of radiogenic He (see text). [f]Water residence times were derived from Equations 3–5, considering a porosity of 1%. [g]Inland samples. Other samples are coastal (W369, W368, LJB-c) or submarine (SMF). [h]Concentrations and isotopic values corrected for admixed seawater based on fractions in Table S3 in Supporting Information S1, and air-saturated seawater values (see text). [i]Values of SMF from Vidal et al. (1981) and air-saturated water values from Capasso and Inguaggiato (1998).

where X is the air-normalized $^4He/^{20}Ne$ ratio of the dissolved gases, $(^4He/^{20}Ne)_{air} = 0.318$, $\beta_{Ne} = 10.62$, and $\beta_{He} = 8.78$ are Bunsen coefficients for the solubility of Ne and He in pure water (Weiss, 1971) assuming that meteoric water recharge occurs at the average temperature of the study area (17°C).

2.3. ⁴He Production Rate and Water Residence Times

To estimate the average ⁴He production rate in the study area, 13 plutonic and volcanic rocks representing the most abundant lithology and chemical composition in the study area were sampled along the ABF (Figure 1b). Rock samples were processed following the Peters and Pettke (2017) methodology. This involved fine milling and pressing powder pills of the samples before measuring the concentrations of major elements and the parent radionuclides U and Th by Laser Ablation Inductively Coupled Plasma Mass Spectrometry (LA-ICP-MS) at the University of Bern, Switzerland (Table S1 in Supporting Information S1). A GeoLas-Pro 193 nm ArF Excimer laser system (Lambda Physik, Göttingen, Germany) was used with an ELAN DRC-e quadrupole mass spectrometer (Perkin Elmer, Waltham, MA, USA). Data were reduced using the SILLS software (Guillong et al., 2008). Average detection limits for SiO_2, Na_2O, K_2O, Th, and U are 0.0001–0.012 μg g⁻¹, and standard deviations of the concentrations are 0.034–0.536.

In crustal rocks, ⁴He is produced from α-decay of ²³⁵U, ²³⁸U, and ²³²Th, and it eventually dissolves into any groundwater present. Therefore, high ⁴He concentrations typify groundwater with long subsurface residence times (Andrews & Lee, 1979). In granitic rocks, the concentrations of U and Th are high, and dissolved ⁴He concentrations may exceed the aqueous solubility of helium (Marine, 1979). Water residence times can be estimated from the ⁴He production rate ($^4He_{pro}$) in the wall rocks along the groundwater flow path and the ⁴He present in the thermal waters in excess of that due to equilibrium with the atmosphere upon recharge (Kulongoski et al., 2008; Torgersen, 1980). This excess ⁴He, corrected for air contamination (cm³ STP g⁻¹ H₂O), is calculated as follows:

$$^4He_{ex} = {}^4He_s - {}^4He_{ASW} - \left({}^{20}Ne_s - {}^{20}Ne_{ASW} \times (He/Ne)_{ASW}\right) \tag{3}$$

where ^4He_s and $^{20}Ne_s$ (cm³ STP g⁻¹ H₂O) are the concentrations measured in the sample, $^4He_{ASW}$ and $^{20}Ne_{ASW}$ are the concentrations in pure air-saturated water at the mean annual recharge temperature of 17°C (4.52×10^{-8} and 1.89×10^{-7} cm³ g⁻¹ H₂O, respectively), and $(He/Ne)_{ASW}$ is the He/Ne ratio in air-saturated water (0.2882, Weiss, 1971). When $^{20}Ne_s < {}^{20}Ne_{ASW}$, Equation 3 reduces to

$$^4He_{ex} = {}^4He_s - {}^4He_{ASW} \times \left({}^{20}Ne_{ASW} / {}^{20}Ne_s \right) \tag{4}$$

The He production rate ($^4He_{pro}$, cm^3 yr^{-1} g^{-1} H$_2$O) is defined as

$$^4He_{pro} = \rho_r \Lambda \times \left(1.19 \times 10^{-13} \times U + 2.88 \times 10^{-14} \times Th \right) \times (1 - \phi)/(\phi) \tag{5}$$

where ρ_r is the bulk density of the wall rock (g cm^{-3}), ϕ is the fracture porosity through which advective water flow occurs, Λ is the fraction of He produced in the rock that is subsequently released into the groundwater (here Λ is assumed to be equal to 1), and U and Th are the uranium and thorium concentrations in the rock (µg g^{-1}), with decay rates of 1.19×10^{-13} and 2.88×10^{-14} cm^3 STP ^{4}He yr^{-1} µg^{-1}, respectively (Kulongoski et al., 2008). To solve Equation 5, we used the average concentrations of 1.2 µg g^{-1} U and 4.9 µg g^{-1} Th in the rocks along the ABF (Table S1 in Supporting Information S1). Ignoring any deep crustal flow entering the system, the water residence time is given by the ratio $^4He_{ex}/^4He_{pro}$ (Equations 3–5).

2.4. Earthquake Hypocenter Depths and Geothermal Gradients

We used a simple approach to estimate the regional geothermal gradients along the ABF, which are essential for understanding the thermal regime of the area and for estimating the fluid circulation depth from solute geo-thermometry. We first analyzed recent earthquake hypocenters to determine the depth to the base of the seismogenic zone, which marks the top of the BDTZ (Aharonov & Scholz, 2019). Then, taking 300 ± 10°C as the approximate temperature at the top of the BDTZ in wet granitic rocks (Aharonov & Scholz, 2019), we calculated geothermal gradients from the derived depths of the BDTZ (Table S2 in Supporting Information S1).

The depth distribution of crustal hypocenters was analyzed according to a well-established methodology similar to previous studies (e.g., Michailos et al., 2020; Zuza & Cao, 2020). The seismic data set is comprised of 190 earthquakes recorded since 2001 (Figure 1b; Data Set S1: "Hypocentral_Depths_dataset.xlsx"). Of these, 116 events with magnitudes of 1.0–3.3 and with hypocentral uncertainties less than 60% were selected from RESNOM (2017). In addition, 74 events with magnitudes of 1.5–2.1 and with hypocentral uncertainties less than 1 km were sourced from Frez et al. (2004). From the normalized cumulative frequency distributions of these hypocenter depths, we determined the 5th and 95th percentiles. We then applied a weighted linear regression to the filtered depth data and to the filtered depth errors and calculated their standard deviations. To evaluate the precision of our analysis, we computed the residuals and standard deviations of the regressions, yielding the uncertainty in the depth of the top of the BDTZ. The Python code for these estimations is provided in Data Set S2 ("Hypocentral_Depths_Analysis.py").

3. Results

3.1. Water Chemistry

Thermal springs are the primary surface expression of geothermal systems along the ABF, with up to six such springs occurring at each site. Table 1 lists the physicochemical parameters of the sampled thermal waters. Toward the northwest along the fault, discharge temperatures increase from 37 to 102°C, while pH decreases from 9.8 to 5.3 (Figure 2b). The total concentrations of dissolved solids (TDS) show a remarkably wide variation, which divides the samples into two geographic groups: inland versus coastal–submarine (Table 1). The inland samples are located far from the ocean (>30 km, Figure 2b) and have a low TDS of 0.3–0.9 g L^{-1}, whereas the coastal–submarine samples are more saline with a TDS of 8–19 g L^{-1}. The coastal–submarine group includes waters from six shallow domestic thermal wells, the coastal thermal anomaly at La Jolla beach (Figure 1c), and the fumarolic submarine field. The solutes in all thermal waters are dominated by Na and Cl, with the coastal–submarine samples exhibiting enrichment in Ca, Li, B (Figure 3a), and SiO$_2$ compared with seawater. All thermal water samples show a strong linear correlation between Na and Cl concentrations ($R^2 = 0.99$; Figure 3b), reflecting binary mixing with seawater. In contrast, Mg concentrations are depleted in the coastal–submarine samples compared to the binary seawater mixing line (Figure 3c), demonstrating that Mg does not behave conservatively.
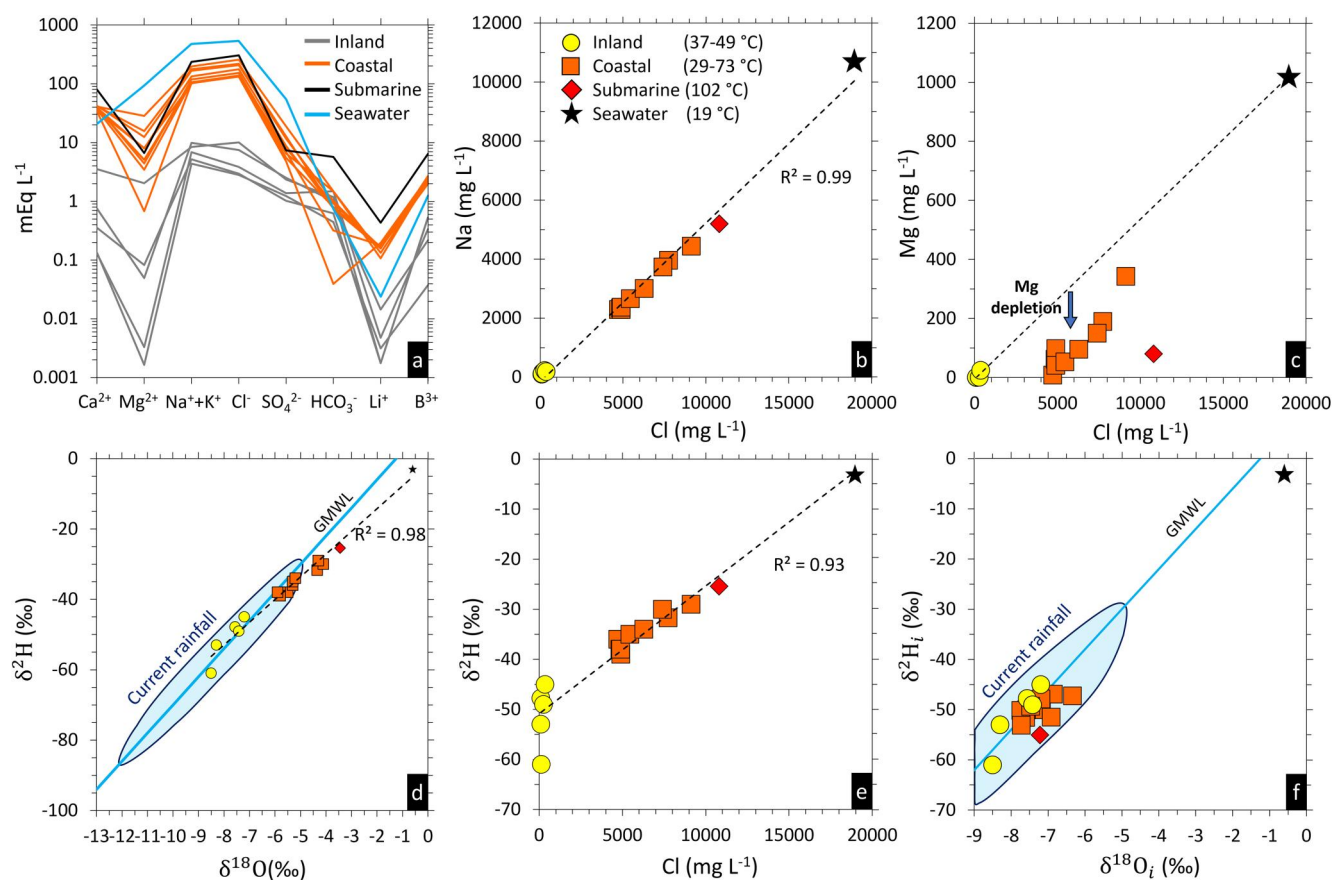
Figure 3. Element and stable O–H isotope correlations in thermal water samples. (a) Schoeller diagram of thermal waters sampled along the Agua Blanca Fault. (b) Sodium versus chlorine concentrations indicating binary mixing between seawater and thermal waters. All thermal water samples were considered in estimating the R^2 value of 0.99. (c) Magnesium versus chlorine concentrations illustrating the Mg depletion of coastal–submarine samples compared to the conservative mixing trend with seawater. (d) Plot of $\delta^{18}O$ versus δ^2H indicating that the thermal waters are of meteoric origin. Current $\delta^{18}O$ and δ^2H values of rainfall in southern California and Baja California are represented by a blue oval (Kretzschmar & Frommen, 2013; Williams & Rodoni, 1997). (e) Plot of δ^2H versus Cl showing that the coastal–submarine waters contain admixed seawater. (f) Initial values of O–H isotopes ($\delta^{18}O_i$ and δ^2H_i), with coastal–submarine waters corrected for the admixture of seawater (see text; exact values provided in Table S3 in Supporting Information S1). GMWL: global meteoric water line (Craig, 1961). Values of $\delta^{18}O$ and δ^2H in deep metamorphic or magmatic fluids typically vary from +5 to +20‰ and −80 to 0‰, respectively (Sheppard, 1986). Thus, both fluid types plot far to the right, outside the scale of panel (f), demonstrating that they do not contribute to the sampled thermal waters.

3.2. Stable O–H Isotopes of Thermal Waters

Values of $\delta^{18}O$ and δ^2H in the thermal water range from −3.5 to −8.5‰ and −25.4 to −61‰, respectively (Table 1). Inland samples fall within the $\delta^{18}O$ and δ^2H ranges of modern rainfall in southern California and Baja California (Kretzschmar & Frommen, 2013; Williams & Rodoni, 1997) and have delta values lower than coastal–submarine samples and local seawater (in which $\delta^{18}O$ is −0.6 and δ^2H is −3.5‰; Figure 3d). Most thermal water samples plot close to the Global Meteoric Water Line (GMWL, Craig, 1961), demonstrating their meteoric origin. The deviation from the GMWL observed for the coastal–submarine waters is consistent with the admixture of seawater, in accord with the correlations between Na and Cl concentrations (Figure 3b) and between δ^2H and Cl values (Figure 3e). The observation that the ratio between Na and Cl concentrations does not precisely match that of seawater (Figure 3b) arises from the non-conservative behavior of Na, caused for instance by the dissolution of feldspars along the flow path. Conversely, as evident in Figure 3e, Cl exhibits a more conservative behavior, defining a clearer signal of seawater admixture.

Other potential sources of fluid in the springs are deep metamorphic or residual magmatic fluids, which typically have $\delta^{18}O$ and δ^2H values of +5 to +20‰ and −80 to 0‰, respectively (Sheppard, 1986). However, even a small contribution from these sources would shift the spring waters to the right of the GMWL in Figure 3f. As no such shift is present, inputs from metamorphic and residual magmatic fluids are ruled out.

To estimate the fraction of admixed seawater (F_{sw}) in the coastal–submarine samples, we assume a binary mixing model:

$$F_{sw} = (Cl_{tw} - Cl_{mw}) / (Cl_{sw} - Cl_{mw}) \tag{6}$$

where Cl_{tw} is the Cl concentration measured in the thermal water sample, and Cl_{mw} and Cl_{sw} are the concentrations of Cl in meteoric water and seawater, respectively. Given the low Cl concentrations in the inland waters, we assume that the meteoric water is Cl-free for this calculation, and we use our measured Cl concentration in local seawater (18,967 mg L^{-1}, Table 1) as a seawater endmember. This mass balance reveals that the coastal–submarine samples contain between 25 and 57 mass% seawater (Table S3 in Supporting Information S1). These fractions allow reconstruction of the initial isotopic signatures of the coastal–submarine samples before their mixing with seawater ($\delta^{18}O_i$ and δ^2H_i), for example, for oxygen:

$$\delta^{18}O_i = \left(\delta^{18}O_{tw} - F_{sw} \times \delta^{18}O_{sw}\right) / (1 - F_{sw}) \tag{7}$$

Figure 3f shows the initial $\delta^{18}O_i$ and δ^2H_i values for the coastal–submarine samples (Table S3 in Supporting Information S1), which are close to the inland thermal waters and the GMWL. The same binary mixing model was used to calculate the theoretical discharge temperature of the thermal springs to correct for cooling caused by the admixture of seawater. This resulted in unmixed discharge temperatures between 33 and 212°C for the coastal–submarine samples (Table S3 in Supporting Information S1).

3.3. Gas Chemistry of Thermal Waters

Nitrogen is the dominant gas dissolved in the thermal waters, with concentrations (1.0–2.3 × 10^{-2} cm^3 STP g^{-1} H$_2$O, Table 2) mostly higher than that in air-saturated water (ASW) (1.2 × 10^{-2} cm^3 STP g^{-1} H$_2$O, Table 2). The volume ratios of N$_2$/Ar in inland and coastal thermal waters (10–38) approach that in ASW (38.6). In contrast, the submarine sample SMF has an N$_2$/Ar ratio of 160. According to Vidal et al. (1982), such a value may originate from the decomposition of nitrogenous compounds in sediments. The second most abundant gas is O$_2$, which has a lower concentration (1.4–25 × 10^{-4} cm^3 STP g^{-1} H$_2$O) than ASW (66 × 10^{-4} cm^3 STP g^{-1} H$_2$O). Depletion in O$_2$ is likely due to its reduction by reaction with wall rocks during deep fluid circulation. Most of the thermal waters have lower CO$_2$ concentrations (0.1–0.3 × 10^{-3} cm^3 STP g^{-1} H$_2$O) than ASW (0.3 × 10^{-3} cm^3 STP g^{-1} H$_2$O). The exceptions are three samples from shallow wells W368, W369, and AJ, which have higher values (4–17 × 10^{-3} cm^3 CO$_2$ STP g^{-1} H$_2$O), presumably due to the microbial activity in the wells.

Concentrations of ^{4}He are in the range 0.6–6.2 × 10^{-6} cm^3 STP g^{-1} H$_2$O (Table 2) and are up to 13–136 times higher than of ASW (4.55 × 10^{-8} cm^3 STP g^{-1} H$_2$O). The volume ratios of ^{4}He/^{20}Ne are 7–92 times higher than those measured in ASW (0.28). The concentrations of ^{4}He and ^{20}Ne in coastal samples were recalculated (Table 2) assuming binary mixing with air-saturated seawater (ASSW) using the He and Ne concentrations in ASSW at 17°C (3.83 × 10^{-8} and 1.60 × 10^{-7} cm^3 g^{-1} H$_2$O; Sano & Takahata, 2005) and the estimated seawater fractions (Table S3 in Supporting Information S1).

The ^{3}He/^{4}He ratios were corrected for air contamination and seawater mixing (R) and normalized to the value of air (denoted R/R_a) varying from 0.06 to 0.94. The coastal samples contained the lowest ^{4}He concentrations (0.6–1.7 × 10^{-6} cm^3 STP g^{-1} H$_2$O), ^{4}He/^{20}Ne ratios (2–5), and R/R_a ratios (0.06–0.26). As helium shows negligible isotopic fractionation during water–gas interaction, the R/R_a value can be used to track the origin of the gas in terms of the air, mantle, and crust endmembers. Figure 3 shows R/R_a versus ^{4}He/^{20}Ne ratios for ASW ($R/R_a = 1$), radiogenic crust ($R_r = (R/R_a)_{radiogenic} = 0.015$, Sano & Wakita, 1985), and the mantle as represented by the Mid-Ocean Ridge Basalt (MORB). For the MORB endmember, we used the highest R/R_a value measured in the Alarcón basin in the nearby Gulf of California ($R_m = (R/R_a)_{MORB} = 8.38$; Castillo et al., 2002). Figure 4a indicates that He dissolved in the thermal waters derives mainly from radiogenic decay.

The fractions of mantle helium (F_m) in the waters were calculated from the R values in Table 2 according to the following equation (modified from Sano & Wakita, 1985):
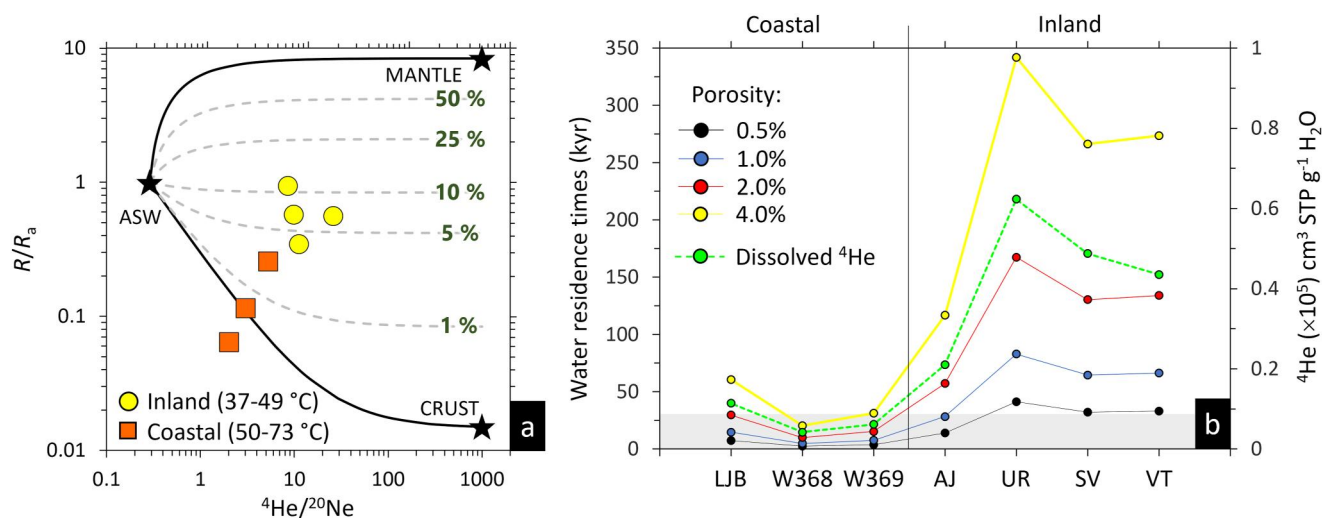
$$F_m = (R - R_r) / (R_r + R_m) \tag{8}$$

Figure 4. Estimation of helium sources and water residence times for inland and coastal thermal waters along the Agua Blanca Fault. (a) Helium-neon isotopic composition (R/Ra vs. $^4He/^{20}Ne$) of the thermal waters, with endmembers representing compositions of the mantle (Castillo et al., 2002), crust (Sano & Wakita, 1985), and air saturated water (ASW) plotted on logarithmic axes. Dashed lines indicate mantle contributions in the samples. (b) Estimated water residence times for several assumed porosity values, with corresponding concentrations of ^4He dissolved in the thermal waters (dashed green line) given on the right-hand y-axis. Note that if the porosity below the LJB site is assumed to be 2% and the porosity below the inland springs is assumed to be 0.5%, then all waters have approximately the same residence time (indicated by gray band).

with the remainder ($1-F_m$) being equal to the fraction of radiogenic helium (F_r). This shows that mantle ^3He makes up less than 11% of the total He in the samples (Figure 4a). Notably, the lowest mantle contributions (0.6%–2.9%) are found in the coastal samples (Table 2). Owing to the lack of ^{20}Ne analyses of the submarine sample SMF (Vidal et al., 1982) and of $^3He/^4He$ analysis of the subaerial sample ST (Zúñiga, 2010), the mantle and radiogenic He contributions in these springs cannot be estimated.

3.4. Water Residence Times

Fracture porosity is an important variable in calculating ^4He-based water residence times from Equations 3–5. Differences in host rock lithologies along the ABF may have some influence on the distribution and magnitude of fracture porosity within the fault, and hence on permeability, but the variability of lithologies in the Alisitos Formation makes it difficult to predict if it would systematically develop higher or lower fracture porosities than the granite. As no hydraulic test results are available from the ABF to constrain porosity values, we simply assumed a plausible range of fracture porosities from 0.5% to 4.0%. This chosen range is comparable to that derived from worldwide borehole hydraulic tests in crystalline rocks (0.1%–2.3%; Stober & Bucher, 2007 and references therein). A fracture porosity of 0.5% yields residence times between 2 and 41 Kyr (Figure 4b), with noticeably shorter residence times for the coastal springs. Conversely, with a fracture porosity of 4%, the residence times are substantially higher (20–342 Kyr) and span a very wide range. Nevertheless, Figure 4b demonstrates that the residence times of water in coastal springs consistently remain lower than those of the inland springs, unless the ratio of their fracture porosities exceeds a factor of approximately three. While the fracture porosity in the Punta Banda coastal system may be higher due to greater fault extension, the very high discharge temperatures at the coast suggest that the thermal waters there indeed have the shortest residence times of all the springs.

3.5. Brittle–Ductile Transition Zone and Geothermal Gradient

The analysis of seismic hypocenters along the ABF demonstrates that the depth to the top of the BDTZ increases systematically from northwest to southeast and is divided into three zones (Figure 5) from 12 ± 0.88 km in the Punta Banda Zone, through 15 ± 0.98 km in the central Santo Tomas—Agua Blanca—Dolores Zone, to 19 ± 1.20 km in the southeastern Trinidad Zone. Considering the complex interplay between topography, stress distribution, and thermal gradients, the observed changes in depth to the BDTZ might reflect influences of the
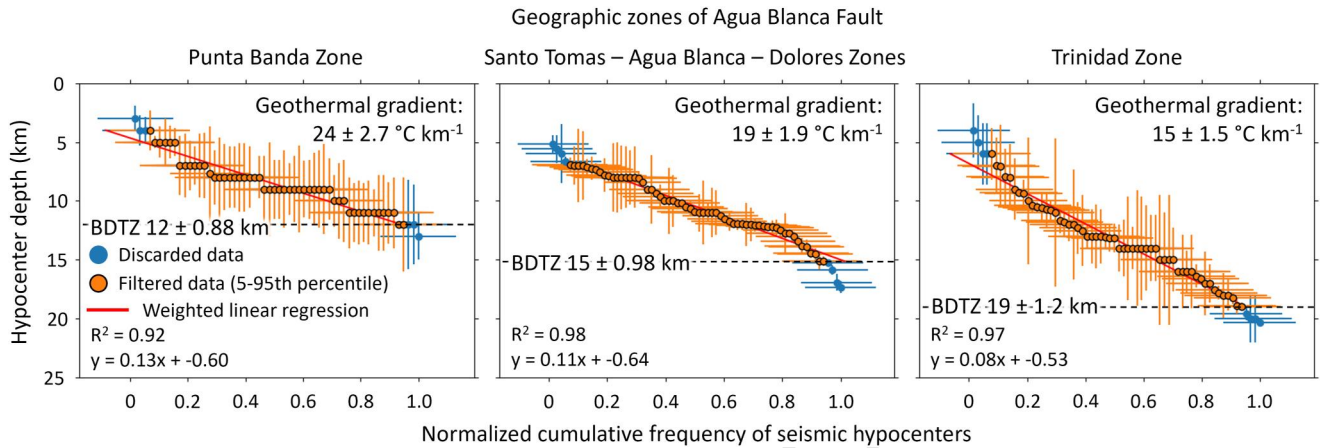
Figure 5. Analysis of seismic hypocenters along the Agua Blanca Fault (see locations of geographic zones in Figure 1b). The 5th to 95th percentiles of the normalized cumulative frequency with depth are shown as orange dots along with their errors (orange lines). Discarded data are represented by blue dots and blue lines. The depth to the 95th percentile is taken to define the top of the brittle–ductile transition zone (BDTZ) in the sense of Aharonov and Scholz (2019).

local topography and associated buoyancy effects. Topographic and buoyancy effects may also extend to the Moho depth, as it correlates positively with the BDTZ depth (Figure 7).

Adopting $300 \pm 10°C$ as the average temperature at the top of the BDTZ in wet granitic rocks (Aharonov & Scholz, 2019), the above depth ranges imply geothermal gradients that decrease progressively from northwest to southeast: $24 \pm 2.7°C\ km^{-1}$ in the Punta Banda Zone, $19 \pm 1.9°C\ km^{-1}$ in Santo Tomas—Agua Blanca—Dolores, and an even lower gradient of $15 \pm 1.5°C\ km^{-1}$ in southeastern Valle Trinidad Zone (Figure 5; Table S2 in Supporting Information S1). The notably low gradient in the Trinidad Zone agrees well with temperature measurements in a borehole located 40 km southeast of the ABF in the San Pedro Mártir range, which indicate a geothermal gradient of $14.9°C\ km^{-1}$ (Smith et al., 1979). Moreover, the trend of decreasing calculated gradients toward the southeast along the entire ABF is in line with regional heat flow studies (e.g., Erkan & Blackwell, 2009). Further, the low magnitudes of the gradients are consistent with the absence of post-Miocene volcanism and with the fact that all local intrusive rocks are older than 90 Ma (Ortega-Rivera, 2003; Storey et al., 1989). The generally low, amagmatic heat flow likely represents a residual effect of the outer arc thermal conditions that existed during the subduction of the Farallon plate, which ended ~30 Ma ago, resulting in a cooling effect on Southern California and Baja California (Erkan & Blackwell, 2009).

3.6. Minimum Temperature and Depth of Water–Rock Equilibration

Since the Peninsular Ranges Batholith of Baja California consists predominantly of tonalite and granodiorite, it can be assumed that the aqueous concentrations of Na, K, and SiO_2 are buffered by reactions with quartz and feldspars at high temperatures. Thus, classical solute geothermometers can provide constraints on the temperatures attained by the thermal waters during their circulation within the ABF system. For the equilibrium

$$\text{Albite} + \text{K}^+ \rightleftharpoons \text{K} - \text{feldspar} + \text{Na}^+ \tag{9}$$
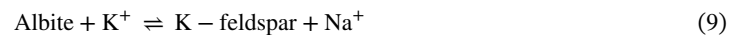
the temperature dependency of the Na/K mass concentration ratio is taken from Giggenbach (1988):

$$T_{\text{Na/K}}\ (°C) = (1390/(1.75 + log(\text{Na/K}))) - 273.15 \tag{10}$$

Similarly, for the quartz equilibrium

$$\text{Quartz} \rightleftharpoons \text{SiO}_{2(\text{aq})} \tag{11}$$

Fournier and Potter (1982) determined the temperature dependency at low to moderate pH values as follows:

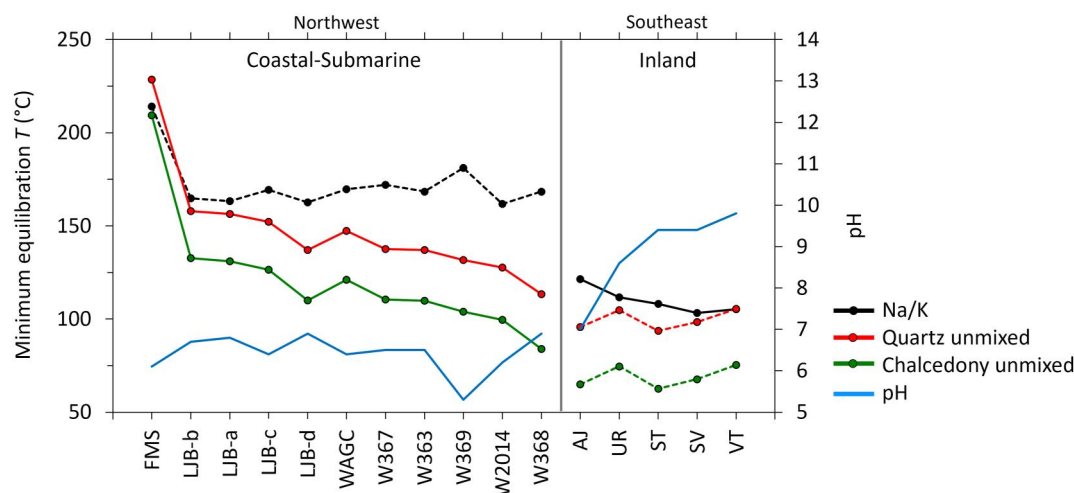**Figure 6.** Minimum temperatures of the thermal waters at depth along the Agua Blanca Fault, from NW to SE, estimated using Na/K and $SiO_{2(aq)}$ geothermometry (see text for interpretation). The pH values measured at the spring discharge temperatures are indicated on the right-hand y axis. Dashed lines link inapplicable geothermometric temperatures (see text for explanation).

$$T_{quartz}\,(°C) = -42.198 + 0.28831[SiO_2] - 3.36686 \times 10^{-4}\,[SiO_2]^2 + 3.1665 \times 10^{-7}\,[SiO_2]^3 + 77.034$$
$$\times \log[SiO_2] \tag{12}$$

Fournier (1977) determined that at lower temperatures (<110°C), other silica phases, such as chalcedony, may control the dissolved silica concentration:

$$T_{chalcedony}\,(°C) = 1032/4.69 - \log[SiO_2] \tag{13}$$

In Equations 12 and 13, $[SiO_2]$ refers to the silica concentration in mg kg_{H2O}^{-1}.

Water–mineral reactions typically slow down during the ascent and cooling of thermal water, causing it to deviate from the equilibrium state. This implies that the metastable solute concentrations measured in surface springs (Table 1) represent their values when the water was last in equilibrium with the buffering minerals (Fournier et al., 1974). Given that reaction kinetics change only gradually and that rock temperatures increase progressively with depth, the reconstructed equilibration temperatures are considered to be minimum estimates.

The minimum equilibration temperatures obtained from the Na/K, quartz, and chalcedony geothermometers are shown in Figure 6. The quartz and chalcedony geothermometers should not be applied to the inland samples (dashed red and green lines in Figure 6) because their pH is up to 9.8, causing an increase in silica solubility that is not captured by the geothermometer calibrations in Equations 12 and 13. On the other hand, in the coastal–submarine thermal waters, the Na/K mass ratios of 13–28 dominantly reflect the admixture of seawater (mass Na/K$_{seawater}$ = 33) rather than buffering by albite and K-feldspar, thereby precluding the application of the Na/K geothermometer (dashed black in Figure 6). To solve the latter issue, we used the quartz and chalcedony geothermometers (Equations 12 and 13) to estimate the equilibration temperature of the coastal–submarine thermal waters. To account for mixing with seawater, we used a binary mixing model with the derived seawater fractions and the seawater SiO_2 concentration of 2.3 mg L^{-1} to estimate the SiO_2 concentration in the thermal endmember water via Equations 12 and 13 (Table S3 in Supporting Information S1).

The minimum equilibrium temperatures for inland geothermal systems are between 103 and 121°C (Na/K geothermometer), increasing from southeast to northwest along the ABF (Figure 6). In contrast, the minimum equilibrium temperatures for the coastal–submarine systems are 84–209°C (chalcedony geothermometer). The hottest values are in the coastal geothermal anomaly in La Jolla beach and the fumarolic submarine field (133 and 209°C, respectively, chalcedony geothermometer).
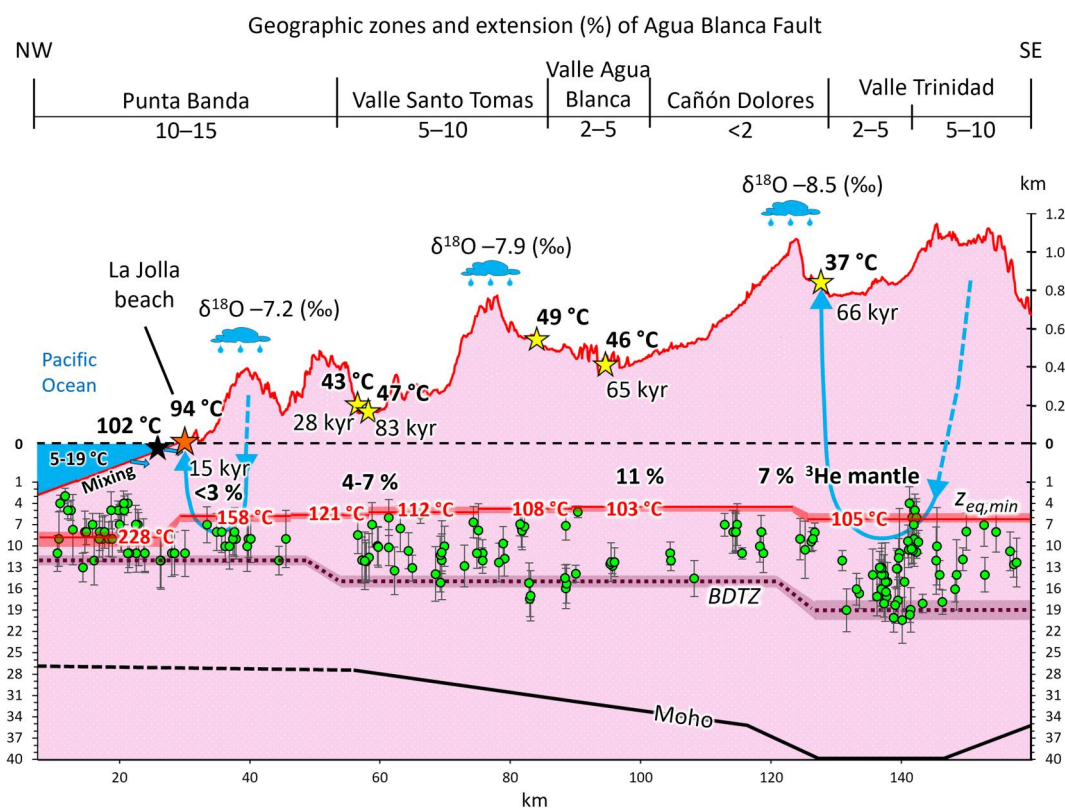
Figure 7. Conceptual model illustrating amagmatic geothermal systems hosted by the Agua Blanca Fault (stars) projected into a NW–SE long section along the main fault trace (red line). Note the differences between the horizontal scale and the two-part vertical scale. Bands at the top indicate extension as a fraction of total displacement (%) along five geographic zones of the fault system (Wetmore et al., 2019). Discharge temperatures (°C), residence times (Kyr), and ^{3}He/He$_{total}$ ratios (%) correlate with the degree of fault extension and with hydraulic head gradient (see text). Green dots denote locations of recent seismic events (Frez et al., 2004; RESNOM, 2017). The red band ($z_{eq,min}$) represents the depth and temperature at which ascending water departs from chemical equilibrium with its wall rocks, as estimated from solute geothermometry (width of band represents the uncertainty of the geothermal gradients). Purple dotted line shows the depth to the top of the brittle–ductile transition zone (BDTZ). The base of the BDTZ is the ultimate depth limit for significant penetration of meteoric water into the crust. Black line represents the depth of Moho (Reyes et al., 2001). Long blue arrows illustrate schematic paths of meteoric water recharging from outside the fault (dashed, projected) and captured at unknown depth by the ABF, then descending through the brittle fault plane (deeper in the SE than in the NW; see text) and then rising to the springs along highly permeable upflow zones.

To estimate the minimum depth at which the thermal waters equilibrated with their wall rocks ($z_{eq,min}$), we used the Na/K temperature for the inland samples and the unmixed quartz temperatures for the coastal–submarine samples (T_{Geot}, Table 1; Table S4 in Supporting Information S1) in combination with Equation 14:

$$z_{eq,min} = (T_{geot} - T_{amb}) / (\Delta T / \Delta z) \qquad (14)$$

where T_{amb} refers to the average ambient temperature (17°C in the Punta Banda zone, 14°C in the central geographic zone, and 10°C in the eastern Valle Trinidad zone) and $\Delta T / \Delta z$ is the local geothermal gradient (24 ± 2.7, 19 ± 1.9 and 15 ± 1.5°C km^{-1} for the three geographic zones; Table S4 in Supporting Information S1). The results (Figure 7; Table S4 in Supporting Information S1) demonstrate that the coastal–submarine samples in the northwest (with discharge temperatures >60°C) have the highest minimum equilibration depths (5.3–10 km), whereas the cooler inland samples in the southeast (with discharge temperatures <50°C) have the lowest minimum equilibration depths (4.2–6.9 km).

It should be noted that choosing the quartz temperature to estimate the equilibration depth of the coastal–submarine samples is arbitrary. Studies of scaling in relatively fast-flowing geothermal wells have shown that

owing to kinetic limitations, quartz only forms at temperatures >180°C, while chalcedony may form down to a temperature of about 110°C (Arnorsson, 1975). However, when the water upflow rate and the reactive fracture surface area are low, such as in long-lived active geothermal systems, quartz can also form below 100°C (Rimstidt & Barnes, 1980; White et al., 1956). Due to the lack of deep samples, we do not know which silica phase controls the SiO_2 concentrations measured in the sampled thermal waters. Consequently, the equilibration depth listed for the coastal–submarine samples (Table S4 in Supporting Information S1) could be up to 1 km less (the equilibration temperature of chalcedony is about 25°C less for the same SiO_2 concentration).

4. Discussion

A conceptual model of the amagmatic orogenic geothermal systems along the ABF, consistent with all geological, geochemical, and geophysical data presented above, is illustrated in Figure 7. The infiltration of meteoric water from elevated topographic regions into the brittle crust, and eventually into the ABF, is driven by hydraulic head gradients and facilitated by fracture networks in the country rock, which are typical of crystalline rocks. Thus, a huge volume of country rock is hydraulically connected to the ABF. As a multicore and multistrand fault with a wide damage zone, the ABF acts as both a barrier and conduit for fluid flow at depth (Caine et al., 1996). Severe grain-size reduction in the core reduces permeability and prevents fluid flow across the fault, but the high fracture density of the surrounding damage zone greatly increases permeability and channels fluid flow along the fault. The relatively high permeability of the ABF, which is subjected to changes in stress through the earthquake cycle may lead to fast siphon-like upflow and then discharge of thermal waters at the surface, such as demonstrated for numerous amagmatic orogenic systems worldwide (e.g., Bucher et al., 2012; Diamond et al., 2018; Ferguson et al., 2023; Forster & Smith, 1988; Ge et al., 2008; Goderniaux et al., 2013; Hubbert, 1940; Stober et al., 2022; Tóth, 1962; Wanner et al., 2020). Variations in permeability and hydraulic head gradients lead to variable water penetration depths of at least a few kilometers, and hence to variable water equilibration temperatures, residence times, and water upflow velocities. Consequently, there is a large range in temperatures (37–102°C) of discharges in topographic lows where the local hydraulic head gradients are highest. Additionally, the long water residence times facilitate changes in the chemical composition of the infiltrated meteoric water due to mineral dissolution and precipitation along its flow path and to mixing with ancient seawater-like porewater in the wall rocks. In the coastal systems, mixing with fresh seawater also occurs. Further details of all these processes are discussed in the following sections.

4.1. Evolution of Chemical Composition Along the Meteoric Water Flow Path

The chlorine concentration in the infiltrated meteoric water along the ABF has increased from its typical original value of <2 mg L^{-1} (Junge & Werby, 1958) to 100–360 mg L^{-1} in the inland thermal springs and to 4,700–11000 mg L^{-1} in the coastal–submarine springs. Water–rock interaction along flow paths is known to increase the concentrations of solutes in infiltrating meteoric water (López & Smith, 1995). Additionally, sea spray may elevate chloride concentrations in meteoric water in the coastal zone and up to 20 km inland (Tsunogai, 1975).

Possible sources of Cl can be constrained by examining the Cl/Br concentration ratios in the spring waters. Along the ABF, the Cl/Br mass ratios are 273–338, close to that of seawater in the study area (280). The inland recharge areas are too far from the coast to be affected by sea spray, but pore spaces in the deep country rocks of the ABF likely contain fossil seawater. Thus, during the migration of meteoric water along fracture networks in the fault system, Cl and Br, and likely also some Na, Mg, SO$_4$, and Li, are assumed to have been acquired by diffusive or advective mixing with seawater-like porewater (e.g., Waber & Smellie, 2008; Waber et al., 2017). Hence, the Cl concentration in the thermal waters depends on their effective cumulative water/rock ratios, which in turn are a function of residence time, path length, porewater chlorinity, volume of accessible pore spaces, and surface area of fractures that allow exchange between the circulating meteoric water and the rock matrix. During the upflow of the heated meteoric water in the coastal area, shallow mixing with modern seawater occurs. Assuming that the chlorinity of the deep waters in the coastal zone was originally similar to that of the inland thermal waters (∼300 mg L^{-1}, Table 1), binary mixing calculations indicate that the coastal springs contain approximately 25%–57% modern seawater.

Other chemical processes that increase the concentration of solutes are mineral dissolution and precipitation reactions along the water flow path, which increase the concentrations of SiO_2, B, Li, F, and Ca. For example, the concentration of SiO_2 leached from feldspars and other silicates is typically controlled by the solubility of either

quartz or chalcedony (Fournier & Potter, 1982; Olguín-Martínez et al., 2022). On the other hand, Li, B and F enrichment are caused by the dissolution of silicate minerals such as biotite, muscovite, and tourmaline or by contributions from highly saline porewater (Drüppel et al., 2020; Seelig & Bucher, 2010; Wanner et al., 2017), and Ca concentrations are controlled by plagioclase weathering and dissolution or by precipitation of secondary calcite (Seyfried & Bischoff, 1979). Finally, the admixture of Mg by seawater in the coastal–submarine thermal waters leads to the precipitation of Mg-bearing sheet silicates (Stober & Bucher, 1999), causing the observed depletion of Mg in the fluid (Figure 3c).

4.2. Infiltration of Meteoric Water and Hydraulic Head Gradients

Stable isotopes of water are fractionated during condensation from cloud vapor. As a result, $\delta^{18}O$ and δ^2H values in rainfall vary in response to effects such as latitude, elevation, distance from the coast, precipitation rate, condensation temperature, and relative humidity (Dansgaard, 1964). In the study area, there is a notably higher precipitation rate in the humid mountainous areas (385–1,050 mm yr^{-1}) than in the valleys or in the semi-arid coastal zone (275 mm yr^{-1}; CICESE, 2019), and average surface temperatures fall from 17°C at the coast to approximately 10°C at 1,000 m a.s.l. Thus, $\delta^{18}O$ values in local surface-water decrease by −0.25‰ per 100 m elevation increase (blue line in Figure 8a; Kretzschmar & Frommen, 2013).

The analyzed inland and unmixed coastal–submarine thermal waters show no systematic shift in $\delta^{18}O$ from the GMWL and have the same stable isotopic signature as current rainfall (Figure 3f). Therefore, the thermal waters must have originally infiltrated as meteoric water under similar climatic conditions in the geological past. This suggests that the variation of $\delta^{18}O$ and δ^2H values of the thermal waters mainly reflects differences in recharge elevation. A first approximation of their mean water recharge elevations can be deduced directly from their $\delta^{18}O$ values (Figure 8a). Thus, all the thermal waters are seen to have infiltrated at mean elevations of 760–1,300 m a.s.l, which are significantly higher than their discharge sites (−30 to 734 m a.s.l). The corresponding mean hydraulic-head differences (Δh) induced by the topographic relief vary within only a small range of ~570–790 m.

Topographic contours corresponding to the mean meteoric recharge elevations in Figure 8a are shown as colored dots in Figure 8b, thereby identifying the recharge catchment for each thermal spring. This shows that meteoric water in the geothermal systems primarily derives from the mountainous landscape to the north of the ABF. In several of the identified catchments, fault segments that host hot springs cut across elevated terrain at the mean recharge elevation (springs SMF, LJB, UR, ST in Figure 8). This opens the possibility that meteoric water could directly infiltrate the fault in these systems. However, this seems to be infeasible for the remaining springs (AJ, SV, VT). We therefore consider it far more likely that the host faults are recharged by rainfall that has fallen over the entire catchment areas. We assume that this rainwater infiltrates into the subsurface and encounters permeable fracture networks typical of crystalline bedrock worldwide. Eventually, this water is captured by the more permeable ABF (Figure 1). We have no knowledge of the nature or permeability of these fracture networks, but the fact that hot chemically evolved meteoric water is discharging in geothermal springs along the ABF is proof that the country rocks are permeable enough to feed the fault. Local rainfall is significant, the surface catchments are large, and according to historical evidence, the discharges of the thermal springs have been consistent over at least the past century (in contrast to the varying discharges of local cold springs). This suggests that enough meteoric water reaches the ABF to keep it saturated and to maintain quasi-steady state flow to the thermal springs. Thus, the permeability of the country rocks and the rainfall rate are not considered to be limiting factors of the flow regime within the ABF.

The depths at which rainwater enters the ABF are also unknown and cannot be estimated from the collected data. Similarly, no maximum infiltration depth of the rainwater can be derived beyond the constraint that it must exceed the $z_{eq.min}$ values of ~4–10 km (red band in Figure 7), which are calculated from combined solute geo-thermometry (Figure 6) and geothermal gradients (Figure 5) via Equation 14. No chemical memory of greater depths is recorded by the spring waters, because chemical equilibrium is likely maintained along the hotter stretches of the flow paths below $z_{eq.min}$ (Diamond et al., 2018; Wanner et al., 2014). In general, the ultimate limit for the penetration of meteoric water by advection is the base of the BDTZ, where dispersed semi-brittle deformation gives way to fully crystal-plastic deformation (e.g., Kohlstedt et al., 1995). This is because the near-hydrostatic water pressures generated by the topographic driving force are too low to hydrofracture the underlying, otherwise impermeable, ductile rocks.
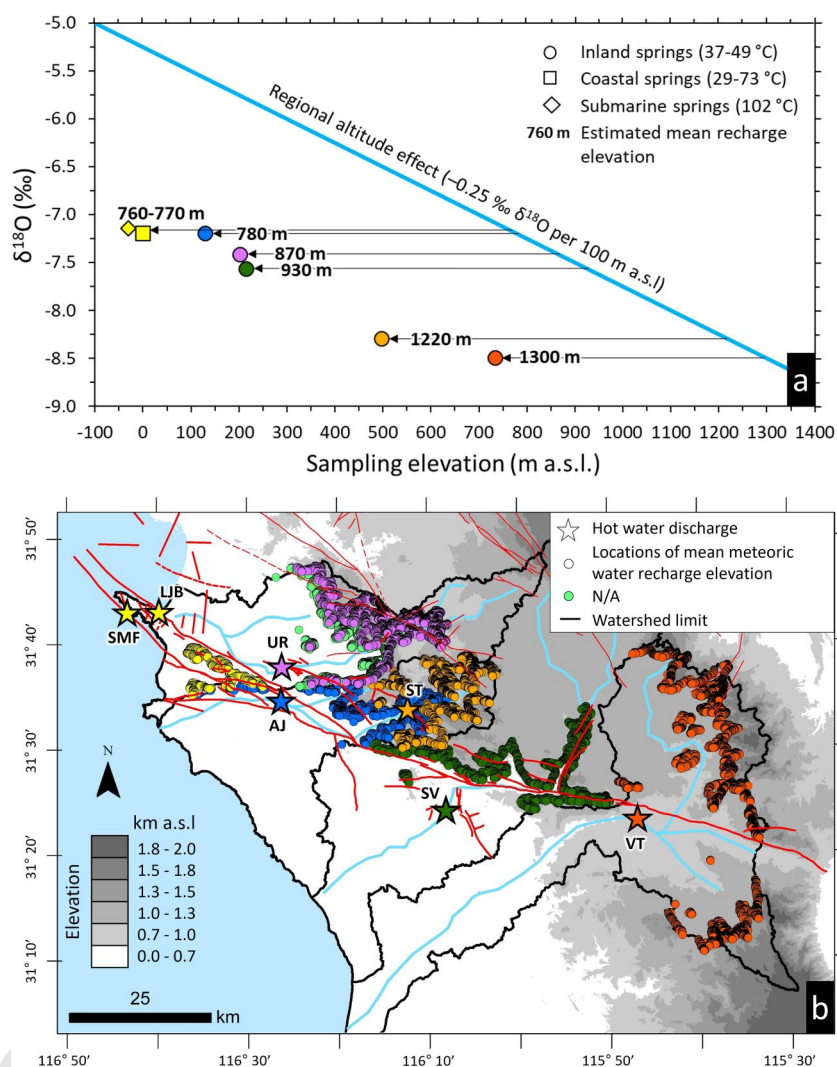
Figure 8. Mean elevation and catchments of meteoric water recharge of geothermal systems along the Agua Blanca Fault. (a) Negative correlation between δ^{18}O values of thermal waters and their sampling elevation compared to that of δ^{18}O in modern surface meteoric water in northern Baja California (blue line; Kretzschmar & Frommen, 2013). The inferred recharge elevation of each thermal water sample is indicated by a labeled arrow. (b) Topographic map of the study area (after INEGI, 2022) displaying thermal water discharge locations (stars) and elevations corresponding to mean meteoric water recharge elevations in the watershed of each cluster of springs (color-coded dots). Perimeters of watersheds (black lines) and rivers (blue lines) dissected by the ABF are also shown. Light green dots (N/A) mark mean water recharge elevations that were excluded from the hydraulic head gradient calculations for springs LJB and SMF (see text).

For the various color-coded geothermal systems, the mean distance (Δx) between the mean meteoric water recharge elevations and the thermal water discharge sites varies from 9 to 23 km (Table S5 in Supporting Information S1; Data Set S3: Recharge_discharge_distances.xlsx). Taking into account the hydraulic-head differences (Δh) between the mean recharge and discharge sites, these distances result in mean hydraulic head gradients ($\Delta h/\Delta x$) of 0.025–0.078. Note that the light green dots in the NW catchment of Figure 8b were omitted in these calculations owing to their great distance from the LJB and SMF springs. Recharge for those springs likely derives from the high topography ($\leq$1,000 m a.s.l.) on the immediately adjacent Punta Banda Peninsula (yellow dots).

4.3. Controls on the Hydraulic and Thermal Behavior of Amagmatic Geothermal Systems

Our study reveals that the hydraulic and thermal behavior of amagmatic orogenic geothermal systems along the ABF is primarily controlled by two main parameters: the permeability of the active upflow zones along the ABF,

and the hydraulic head gradient generated by the high-relief topography mainly to the north of the fault (Figure 2). Assuming that the rate of meteoric precipitation and the fracture permeability of the country rock does not limit the deep fluid circulation (Section 4.2), which is a prerequisite for the deep single-pass fluid circulation (Alt-Epping et al., 2021) postulated in our conceptual model (Figure 7), then these two parameters determine all key features of the flow system. This includes the locations and temperatures of hot springs at the surface, the rate of water upflow, the depth of meteoric water penetration, the temperature and depth of water–rock equilibration, the subsurface water residence times, and probably also the $^3He/He_{total}$ fractions.

The importance of fault zone permeability in controlling the flow systems is manifested by the observation that all thermal waters discharge within the highly fractured and hence permeable ABF system (Figure 2a). Discharge sites are located at low elevations, such as valley floors or along the coast, highlighting the role of the hydraulic head gradient in controlling the location of the discharge sites. However, plotting the estimated hydraulic head gradients against the unmixed discharge temperatures does not yield a clear correlation (Figure 9a), indicating that the hydraulic head gradient does not directly control the upflow rates and discharge temperatures in the studied geothermal systems.

In contrast, there appears to be a strong correlation between permeability and discharge temperatures (Figure 9b). The degree of extension along the ABF, determined from geodetic data and normalized such that the lateral and heave components sum to a total of 100% of the horizontal slip vector (Wetmore et al., 2019), is used as a proxy for permeability variations. Higher extension of a fault creates higher fracture porosity, which can increase the permeability of the system. Figure 9b shows that an increase in fault extension is associated with an increase in water discharge temperature. For instance, the Punta Banda segment, which is located at the coast and characterized by the highest degree of extension (10%–15%, Figure 9b), shows extremely high discharge temperatures ($T_{unmixed}$: 144–212°C), suggesting the presence of highly permeable upflow zones. Together with the lack of correlation between hydraulic head gradients and discharge temperatures (Figure 9a), this implies that the fault permeability constitutes the first-order control on upflow rates and discharge temperatures and thus on the magnitudes of the resulting thermal anomalies of hot but almost dry rocks in the surrounding rocks.

Application of general hydrogeologic principles (Zijl, 1999) predicts that meteoric water penetrates to greater depths with increasing horizontal length (Δx) between recharge and discharge sites. For instance, numerical simulations of a fault-hosted orogenic geothermal system in the Swiss Alps have shown that a length/depth ratio of about 1.1 is required for single-pass flow through a fault with elevated permeability ($>10^{-15}$ m^2), such as inferred for the ABF, including the counteractive buoyancy induced by a 25°C km^{-1} geothermal gradient (Alt-Epping et al., 2021). Along the ABF, mean Δx is estimated to vary between 9 and 23 km (Section 4.2). Considering that the ultimate depth limit for significant advective flow of meteoric water into the crust is the base of the BDTZ (Section 4.2), the scope for deep penetration is greatest in the southeastern inland segment of the fault, where the BDTZ lies 15–19 km deep, compared to the northwestern coastal segment where the BDT is only 12 km deep (Figure 7). Accordingly, the low hydraulic head gradients ($\Delta h/\Delta x$) in the inland systems of the ABF may induce deeper penetration of meteoric water, such that it is heated to higher temperatures than in the coastal systems. However, due to the lower inferred fault permeability and geothermal gradient in the eastern zone, Darcy's Law predicts that the rate of water upflow must be slower too. As water–rock reaction rates depend on the flow rate, the depth at which the ascending water departs from chemical equilibrium with the surrounding rocks is shallower in the southeast than in the coastal zones (Figure 9d). This explains the shallower minimum depths of penetration inferred from the equilibrium geothermometric results for the southeastern springs. Thus, while the hydraulic head gradient may not strongly impact upflow rates and discharge temperatures, it exerts significant control over the water infiltration depth and the depth of water–rock equilibration.

Previous work has proposed that the helium isotope signatures of the thermal springs can be attributed to the migration of fluids derived from the mantle through permeable faults, combined with the modification of the mantle $^3He/^4He$ ratio by mixing with radiogenic helium (Barry et al., 2020; Polyak et al., 1991). The inverse correlation between the hydraulic head gradient and the $^3He/He_{total}$ ratio observed in the present study (Figure 9c) suggests that longer and deeper water flow paths enable greater acquisition of ^3He. Moreover, the deeper and more extensive water infiltration along the eastern ABF is consistent with the longer estimated water residence times (Figure 9e). Analyzing the variation of recharge elevation and the lack of correlation between residence time and geographic location along the inland portion of the ABF, it becomes evident that there are multiple isolated flow compartments. This suggests the presence of low permeability zones along the ABF, which hinder
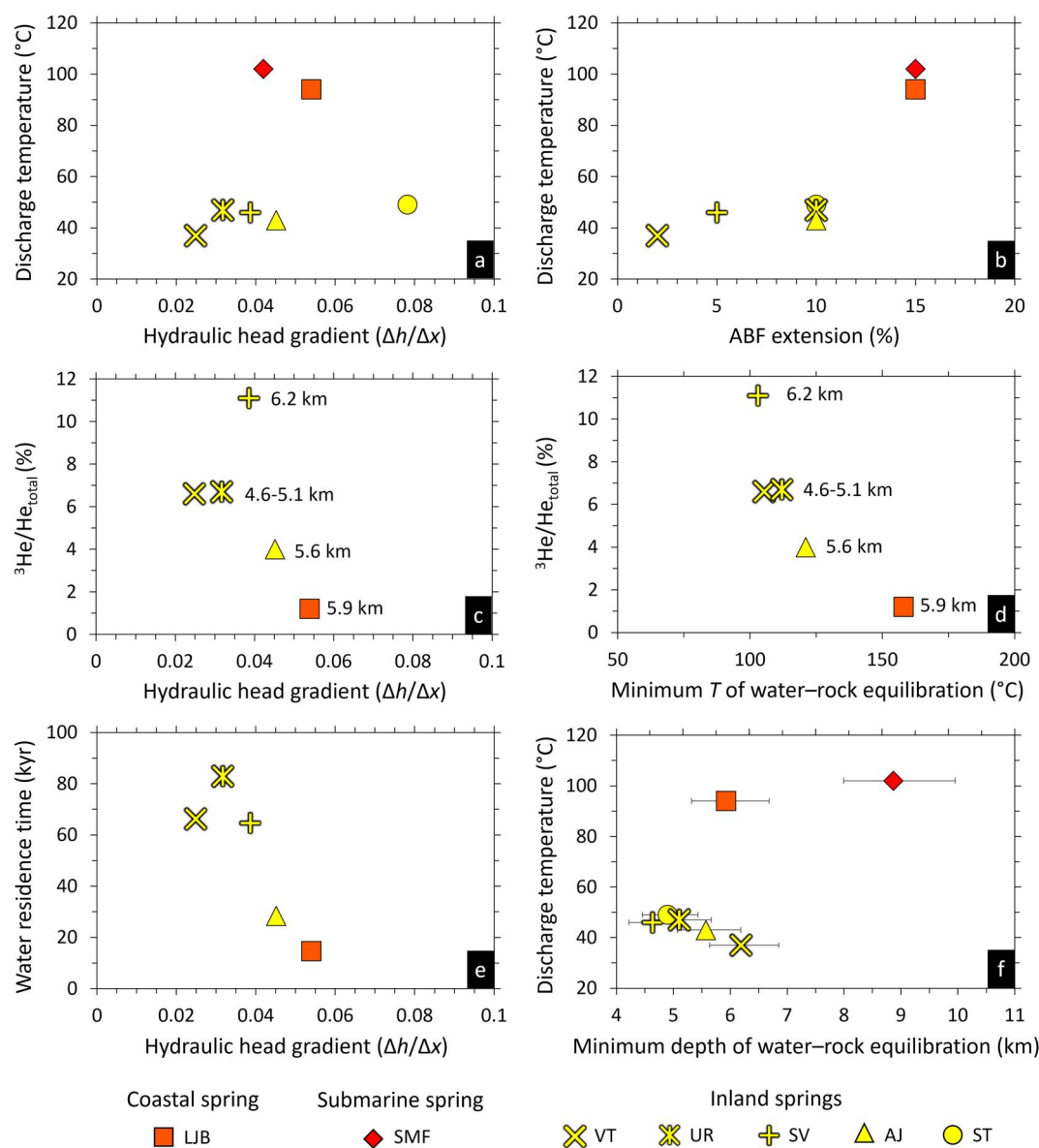
Figure 9. Correlations between key parameters characterizing the flow systems of the amagmatic geothermal systems along the Agua Blanca Fault. (a) Discharge temperature versus hydraulic head gradient, revealing no significant correlation. The plotted discharge temperatures have been adjusted to account for the cooling influence of recent seawater admixture (Table S3 in Supporting Information S1). (b) Discharge temperature versus ABF extension (proxy of permeability), demonstrating a strong positive correlation between these variables. (c) ^{3}He/He$_{total}$ versus hydraulic head gradient, with km labels indicating minimum water penetration depths based on geothermometry. (d) ^{3}He/He$_{total}$ versus minimum temperature of water–rock equilibration, with km labels indicating the corresponding minimum depths of equilibration. Plots c and d show that thermal waters with shallower depths of water–rock equilibration and lower discharge temperatures (corresponding to lower upflow rates) exhibit higher ^{3}He fractions. (e) Water residence time versus hydraulic head gradient, illustrating strong control of hydraulic head gradient on residence time. The plotted water residence times are estimated assuming a porosity of 1%. (f) Discharge temperature versus minimum depth of water–rock equilibration.

connection between adjacent flow compartments. The existence of these low permeability zones further confirms the strong influence of local permeability on flow rates.

The observed inverse relationship between discharge temperature and inferred minimum infiltration depth (Figure 9f) suggests that ultradeep advective infiltration (>>10 km), such as is feasible in the inland systems, is not a prerequisite for amagmatic systems to achieve temperatures above 120°C in the shallow subsurface. The only

requirements are that the local geothermal gradient allows the water to exceed this temperature threshold at depth (e.g., Diamond et al., 2018) and that the upflow rates are high (e.g., Wanner et al., 2019). In the coastal zone, these conditions are met, with meteoric water reaching a temperature of at least 160°C at a depth of 6 km (Figure 9f). Temperatures in the plume of hot water ascending to the coastal springs are probably above 120°C at <2 km depth.

5. Summary and Conclusions

We have investigated the behavior of amagmatic orogenic geothermal systems along the ABF in Baja California using a multidisciplinary approach encompassing geochemical, geophysical, and geological data. Our findings, consistent with similar orogenic faults worldwide, demonstrate that these systems arise from gravity-driven infiltration of meteoric water that is precipitating on the high-relief hinterland of the fault. During its penetration deep into the brittle fault plane, the meteoric water increases its temperature along the local geothermal gradient while acquiring salinity and helium due to interactions with the wall rocks and with saline porewater (residual seawater) along its flow path. Our data provide strong evidence that the flow characteristics of these systems, including water upflow rates, discharge temperatures, temperatures and depths of water-rock equilibration, water residence times, and ^{3}He/He$_{total}$ fractions, are primarily controlled by the variability of the hydraulic head gradient and the permeability of the upflow zones along the ABF. The hottest spring waters (up to 102°C), which have the fastest flow rates, discharge on the Pacific coast where fault extension is highest (10%–15%) and hence permeability is highest. The hydraulic head gradient plays a key role in determining water flow pathways, including the depth of infiltration, water residence times, and ^{3}He/He$_{total}$ fractions. The recharge rate and permeability of the country rocks do not appear to be limiting factors in this system.

Our results demonstrate that, under favorable conditions characterized by high fault permeability and high hydraulic head gradients, the temperature threshold for electricity production (∼120°C) in amagmatic geothermal systems can be reached at relatively shallow depths (<4 km). This confirms their potential not only for the exploitation of hot discharging water but also for sustainable EGS exploitation of the hot rocks that surround the water upflow zones. Based on our findings, future exploration for orogenic geothermal systems should prioritize valley floors intersected by active regional faults, as these locations tend to exhibit maximum values of hydraulic head gradients and upflow rates. Overall, our study sheds light on the dynamics and controls of amagmatic orogenic geothermal systems, providing insights for both scientific research and practical applications in the field of geothermal energy exploration and development.

Data Availability Statement

All the geological, geochemical and geophysical data on which this research is based are publicly available at the Zenodo repository Carbajal-Martínez et al. (2023) (https://doi.org/10.5281/zenodo.8160873).

Abbreviations

ABF   Agua Blanca Fault
BDTZ   brittle ductile transition zone
ASW   air saturated water

References

Aharonov, E., & Scholz, C. H. (2019). The Brittle-Ductile transition predicted by a physics-based friction law. *Journal of Geophysical Research: Solid Earth*, *124*(3), 2721–2737. https://doi.org/10.1029/2018JB016878

Allen, C. R., Silver, L. T., & Stehli, F. G. (1960). Agua Blanca Fault—A major transverse structure of northern Baja California, Mexico. *Bulletin of the Geological Society of America*, *71*(4), 467–482. https://doi.org/10.1130/0016-7606(1960)71[467:ABFMTS]2.0.CO;2

Alt-Epping, P., Diamond, L. W., & Wanner, C. (2022). Permeability and groundwater flow dynamics in deep-reaching orogenic faults estimated from regional-scale hydraulic simulations. *Geochemistry, Geophysics, Geosystems*, *23*(12), e2022GC010512. https://doi.org/10.1029/2022gc010512

Alt-Epping, P., Diamond, L. W., Wanner, C., & Hammond, G. E. (2021). Effect of glacial/interglacial recharge conditions on flow of meteoric water through deep orogenic faults: Insights into the geothermal system at Grimsel Pass, Switzerland. *Journal of Geophysical Research: Solid Earth*, *126*(7), 1–21. https://doi.org/10.1029/2020JB021271

Andrews, J. N., & Lee, D. J. (1979). Inert gases in groundwater from the Bunter Sandstone of England as indicators of age and palaeoclimatic trends. *Journal of Hydrology*, *41*(3–4), 233–252. https://doi.org/10.1016/0022-1694(79)90064-7

Arango-Galván, C., Prol-Ledesma, R. M., Flores-Márquez, E. L., Canet, C., & Villanueva Estrada, R. E. (2011). Shallow submarine and subaerial, low-enthalpy hydrothermal manifestations in Punta Banda, Baja California, Mexico: Geophysical and geochemical characterization. *Geothermics*, *40*(2), 102–111. https://doi.org/10.1016/j.geothermics.2011.03.002

Arnorsson, S. (1975). Application of the silica geothermometer in low temperature hydrothermal areas in Iceland. *American Journal of Science*, *275*(7), 763–784. https://doi.org/10.2475/ajs.275.7.763

Asta, M. P., Gimeno, M. J., Auqué, L. F., Gómez, J., Acero, P., & Lapuente, P. (2010). Secondary processes determining the pH of alkaline waters in crystalline rock systems. *Chemical Geology*, *276*(1–2), 41–52. https://doi.org/10.1016/j.chemgeo.2010.05.019

Barry, P. H., Negrete-Aranda, R., Spelz, R. M., Seltzer, A. M., Bekaert, D. V., Virrueta, C., & Kulongoski, J. T. (2020). Volatile sources, sinks and pathways: A helium-carbon isotope study of Baja California fluids and gases. *Chemical Geology*, *550*, 119722. https://doi.org/10.1016/j.chemgeo.2020.119722

Beltrán-Abaunza, J. M., & Quintanilla-Montoya, A. L. (2001). Calculated heat flow for the Ensenada region, Baja California, Mexico. *Ciencias Marinas*, *27*(4), 619–634. https://doi.org/10.7773/cm.v27i4.497

Bucher, K., Stober, I., & Seelig, U. (2012). Water deep inside the mountains: Unique water samples from the Gotthard rail base tunnel, Switzerland. *Chemical Geology*, *334*, 240–253. https://doi.org/10.1016/j.chemgeo.2012.10.031

Caine, J. S., Evans, J. P., & Forster, C. B. (1996). Fault zone architecture and permeability structure. *Geology*, *24*(11), 1025–1028. https://doi.org/10.1130/0091-7613(1996)024<1025:FZAAPS>2.3.CO;2

Capasso, G., & Inguaggiato, S. (1998). A simple method for the determination of dissolved gases in natural waters. An application to thermal waters from Vulcano Island. *Applied Geochemistry*, *13*(5), 631–642. https://doi.org/10.1016/S0883-2927(97)00109-1

Carbajal-Martínez, D., Peiffer, L., Hinojosa-Corona, A., Trasviña-Castro, A., Arregui-Ojeda, S. M., Carranza-Chávez, F. J., et al. (2020). UAV-based thermal imaging and heat output estimation of a coastal geothermal resource: La Jolla beach, Baja California, Mexico. *Renewable Energy*, *168*, 1364–1373. https://doi.org/10.1016/j.renene.2020.12.113

Carbajal-Martínez, D., Wanner, C., Diamond, L. W., Peiffer, L., Fletcher, J. M., Inguaggiato, C., & Contreras-López, M. (2023). Behavior of amagmatic orogenic geothermal systems: Insights from the Agua Blanca Fault, Baja California, Mexico [Dataset]. *Zenodo*. https://doi.org/10.5281/zenodo.8160873

Castillo, P. R., Hawkins, J. W., Lonsdale, P. F., Hilton, D. R., Shaw, A. M., & Glascock, M. D. (2002). Petrology of Alarcon Rise lavas, Gulf of California: Nascent intracontinental ocean crust. *Journal of Geophysical Research*, *107*(B10), ECV5-1–ECV5-15. https://doi.org/10.1029/2001jb000666

Chen, C. H. (1985). Chemical characteristics of thermal waters in the central range of Taiwan, R.O.C. *Chemical Geology*, *49*(1–3), 303–317. https://doi.org/10.1016/0009-2541(85)90163-9

CICESE. (2019). Datos climáticos diarios del CLICOM del SMN a través de su plataforma web del CICESE. Retrieved from http://clicom-mex.cicese.mx/

Coussens, J., Woodman, N., Upton, P., Menzies, C. D., Janku-Capova, L., Sutherland, R., & Teagle, D. A. H. (2018). The significance of heat transport by shallow fluid flow at an active plate boundary: The Southern Alps, New Zealand. *Geophysical Research Letters*, *45*(19), 10323–10331. https://doi.org/10.1029/2018GL078692

Craig, H. (1961). Isotopic variations in meteoric waters. *Science*, *133*(3465), 1702–1703. https://doi.org/10.1126/science.133.3465.1702

Dansgaard, W. (1964). Stable isotopes in precipitation. *Tellus*, *16*(4), 436–468. https://doi.org/10.3402/tellusa.v16i4.8993

Diamond, L. W., Wanner, C., & Waber, H. N. (2018). Penetration depth of meteoric water in orogenic geothermal systems. *Geology*, *46*(12). https://doi.org/10.1130/G45394.1

Drüppel, K., Stober, I., Grimmer, J. C., & Mertz-Kraus, R. (2020). Experimental alteration of granitic rocks: Implications for the evolution of geothermal brines in the Upper Rhine Graben, Germany. *Geothermics*, *88*, 101903. https://doi.org/10.1016/j.geothermics.2020.101903

Erkan, K., & Blackwell, D. (2009). Transient thermal regimes in the Sierra Nevada and Baja California extinct outer arcs following the cessation of Farallon subduction. *Journal of Geophysical Research*, *114*(2), 1–18. https://doi.org/10.1029/2007JB005498

Ferguson, G., McIntosh, J., Warr, O., & Sherwood Lollar, B. (2023). The low permeability of the Earth's Precambrian crust. *Communications Earth and Environment*, *4*(1), 1–8. https://doi.org/10.1038/s43247-023-00968-2

Forster, C., & Smith, L. (1988). Groundwater flow systems in mountainous terrain: 1. Numerical modeling technique. *Water Resources Research*, *24*(7), 999–1010. https://doi.org/10.1029/WR024i007p00999

Fournier, R. O. (1977). Chemical geothermometers and mixing models for geothermal systems. *Geothermics*, *5*(1–4), 41–50. https://doi.org/10.1016/0375-6505(77)90007-4

Fournier, R. O., & Potter, I. R. W. (1982). An equation correlating the solubility of quartz in water from 25° to 900°C at pressures up to 10,000 bars. *Geochimica et Cosmochimica Acta*, *46*(10), 1969–1973.

Fournier, R. O., White, D. E., & Truesdell, A. H. (1974). Geochemical indicator of subsurface temperature: Part 1, basic assumptions. *Journal of Research of the US Geological Survey*, *2*(3), 259–262.

Frez, J., Acosta, J., Nava, A., Suarez, F., Gonzalez, J., Arellano, G., et al. (2004). *Microseismicity studies in northern Baja California, Mexico: The Agua Blanca Fault*. AGU. Retrieved from https://ui.adsabs.harvard.edu/abs/2004AGUFM.S51A0129F/abstract

Gastil, G., & Bertine, K. (1986). Correlation between seismicity and the distribution of thermal and carbonate water in southern and Baja California, United States and Mexico. *Geology*, *14*(4), 287–290. https://doi.org/10.1130/0091-7613(1986)14<287:CBSATD>2.0.CO;2

Gastil, R. G., Phillips, R. P., & Allison, E. C. (1975). *Reconnaissance geology of the state of Baja California*. Geological Society of America, 140, In: Colorado.

Ge, S., Wu, Q. B., Lu, N., Jiang, G. L., & Ball, L. (2008). Groundwater in the Tibet Plateau, western China. *Geophysical Research Letters*, *35*(18), 1–5. https://doi.org/10.1029/2008GL034809

Giggenbach, W. F. (1988). Geothermal solute equilibria. Derivation of Na-K-Mg-Ca geoindicators. *Geochimica et Cosmochimica Acta*, *52*(12), 2749–2765. https://doi.org/10.1016/0016-7037(88)90143-3

Goderniaux, P., Davy, P., Bresciani, E., De Dreuzy, J. R., & Le Borgne, T. (2013). Partitioning a regional groundwater flow system into shallow local and deep regional flow compartments. *Water Resources Research*, *49*(4), 2274–2286. https://doi.org/10.1002/wrcr.20186

Gold, P. O., Behr, W. M., Fletcher, J. M., Rockwell, T. K., & Figueiredo, P. M. (2020). Time-invariant late quaternary slip rates along the Agua Blanca Fault, northern Baja California, Mexico. *Tectonics*, *39*(9), 1–26. https://doi.org/10.1029/2019TC005788

Grasby, S. E., & Hutcheon, I. (2001). Controls on the distribution of thermal springs in the southern Canadian Cordillera. *Canadian Journal of Earth Sciences*, *38*(3), 427–440. https://doi.org/10.1139/e00-091

Guillong, M., Meier, D. L., Allan, M. M., Heinrich, C. A., & Yardley, B. W. D. (2008). *SILLS: A Matlab-based program for the reduction of laser ablation ICP–MS data of homogeneous materials and inclusions* (Vol. 40, pp. 328–333). Mineralogical Association of Canada Short Course.

Hamme, R. C., & Emerson, S. R. (2004). The solubility of neon, nitrogen and argon in distilled water and seawater. *Deep-Sea Research Part I Oceanographic Research Papers*, *51*(11), 1517–1528. https://doi.org/10.1016/j.dsr.2004.06.009

Hilton, D. R. (1996). The helium and carbon isotope systematics of a continental geothermal system: Results from monitoring studies at Long Valley caldera (California, U.S.A.). *Chemical Geology*, *127*(4), 269–295. https://doi.org/10.1016/0009-2541(95)00134-4

Hubbert, K. M. (1940). The theory of ground-water motion. *The Journal of Geology*, *47*(8).

INEGI. (2022). Continuo de Elevaciones Mexicano (CEM). Retrieved from https://sinegi.page.link/1av6

Inguaggiato, S., & Rizzo, A. (2004). Dissolved helium isotope ratios in ground-waters: A new technique based on gas-water re-equilibration and its application to Stromboli volcanic system. *Applied Geochemistry*, *19*(5), 665–673. https://doi.org/10.1016/j.apgeochem.2003.10.009

Junge, C. E., & Werby, R. T. (1958). The concentration of chloride, sodium, potassium, calcium, and sulfate in rain water over the United States. *Journal of Meteorology*, *15*(5), 417–425. https://doi.org/10.1175/1520-0469(1958)015<0417:tcocsp>2.0.co;2

Kohlstedt, D. L., Evans, B., & Mackwell, S. J. (1995). Strength of the lithosphere: Constraints imposed by laboratory experiments. *Journal of Geophysical Research*, *100B*(B9), 17587–17602. https://doi.org/10.1029/95JB01460

Kretzschmar, T. G., & Frommen, T. (2013). Stable Isotope Composition of Surface and Groundwater in Baja California, Mexico. *Procedia Earth and Planetary Science*, *7*, 451–454. https://doi.org/10.1016/j.proeps.2013.03.194

Kulongoski, J. T., Hilton, D. R., Cresswell, R. G., Hostetler, S., & Jacobson, G. (2008). Helium-4 characteristics of groundwaters from Central Australia: Comparative chronology with chlorine-36 and carbon-14 dating techniques. *Journal of Hydrology*, *348*(1–2), 176–194. https://doi.org/10.1016/j.jhydrol.2007.09.048

López, D. L., & Smith, L. (1995). Fluid flow in fault zones: Analysis of the interplay of convective circulation and topographically driven groundwater flow. *Water Resources Research*, *31*(6), 1489–1503. https://doi.org/10.1029/95WR00422

López, D. L., & Smith, L. (1996). Fluid flow in fault zones: Influence of hydraulic anisotropy and heterogeneity on the fluid flow and heat transfer regime. *Water Resources Research*, *32*(10), 3227–3235. https://doi.org/10.1029/96WR02101

Marine, I. W. (1979). The use of naturally occurring helium to estimate groundwater velocities for studies of geologic storage of radioactive waste. *Water Resources Research*, *15*(5), 1130–1136. https://doi.org/10.1029/WR015i005p01130

McCaig, A. M. (1988). Deep fluid circulation in fault zones. *Geology*, *16*(10), 867–870. https://doi.org/10.1130/0091-7613(1988)016<0867:DFCIFZ>2.3.CO;2

Menzies, C. D., Teagle, D. A. H., Craw, D., Cox, S. C., Boyce, A. J., Barrie, C. D., & Roberts, S. (2014). Incursion of meteoric waters into the ductile regime in an active orogen. *Earth and Planetary Science Letters*, *399*, 1–13. https://doi.org/10.1016/j.epsl.2014.04.046

Menzies, C. D., Teagle, D. A. H., Niedermann, S., Cox, S. C., Craw, D., Zimmer, M., et al. (2016). The fluid budget of a continental plate boundary fault: Quantification from the Alpine Fault, New Zealand. *Earth and Planetary Science Letters*, *445*, 125–135. https://doi.org/10.1016/j.epsl.2016.03.046

Michailos, K., Sutherland, R., Townend, J., & Savage, M. K. (2020). Crustal thermal structure and exhumation rates in the Southern Alps near the central Alpine Fault, New Zealand. *Geochemistry, Geophysics, Geosystems*, *21*(8), e2020GC008972. https://doi.org/10.1029/2020GC008972

Olguín-Martínez, M. G., Peiffer, L., Dobson, P. F., Spycher, N., Inguaggiato, C., Wanner, C., et al. (2022). PyGeoT: A tool to automate mineral selection for multicomponent geothermometry. *Geothermics*, *104*, 102467. https://doi.org/10.1016/j.geothermics.2022.102467

Ortega-Rivera, A. (2003). *Geochronological constraints on the tectonic history of the Peninsular Ranges batholith of Alta and Baja California: Tectonic implications for western México*. Geological Society of America Special Paper, 372, 297–335. https://doi.org/10.1130/0-8137-2374-4.297

Ortega-Rivera, A., Suárez-Vidal, F., Mendoza-Borunda, R., & de la O, M. (2018). A multidisciplinary approach to estimate slip rate-magnitude and recurrence time for a segment of a major active fault. Case study: The Agua Blanca Fault, Valle de Agua Blanca, B.C., México. *Journal of South American Earth Sciences*, *88*, 1–15. https://doi.org/10.1016/j.jsames.2018.08.005

Peters, D., & Pettke, T. (2017). Evaluation of Major to Ultra Trace Element Bulk Rock Chemical Analysis of Nanoparticulate Pressed Powder Pellets by LA-ICP-MS. *Geostandards and Geoanalytical Research*, *41*(1), 5–28. https://doi.org/10.1111/ggr.12125

Polyak, B. G., Kononov, V. I., Fernandez, R., Kamenskiy, I. L., & Zinkevich, V. P. (1991). Helium isotopes in thermal fluids of Baja California and adjacent areas. *International Geology Review*, *33*(12), 1218–1232. https://doi.org/10.1080/00206819109465747

RESNOM. (2017). Red Sísmica del Noroeste de México. https://doi.org/10.7914/SN/BC

Reyes, L. M., Rebollar, C. J., & Castro, R. (2001). Depth of the Moho in northern Baja California using (Pg-Pn) travel times. *Geofísica Internacional*, *40*(1), 21–29. https://doi.org/10.22201/igeof.00167169p.2001.40.1.417

Rimstidt, J. D., & Barnes, H. L. (1980). The kinetics of silica-water reactions. *Geochimica et Cosmochimica Acta*, *44*(11), 1683–1699. https://doi.org/10.1016/0016-7037(80)90220-3

Rockwell, T. K., Muhs, D. R., Kennedy, G. L., Hatch, M. E., Wilson, S. M., & Klinger, R. E. (1989). *Uranium-series ages, faunal correlations and tectonic deformation of marine terraces within the Agua Blanca fault zone at Punta Banda, northern Baja California, Mexico*. Los Angeles, Society of Economic Paleontologists and Mineralogists, 1–16.

Sano, Y., & Takahata, N. (2005). Measurement of noble gas solubility in seawater using a quadrupole mass spectrometer. *Journal of Oceanography*, *61*(3), 465–473. https://doi.org/10.1007/s10872-005-0055-x

Sano, Y., & Wakita, H. (1985). Geographical distribution of He3/He4 ratios in Japan: Implications for arc tectonics and incipient magmatism. *Journal of Geophysical Research*, *90*(B10), 8729–8741. https://doi.org/10.1029/JB090iB10p08729

Seelig, U., & Bucher, K. (2010). Halogens in water from the crystalline basement of the Gotthard rail base tunnel (central Alps). *Geochimica et Cosmochimica Acta*, *74*(9), 2581–2595. https://doi.org/10.1016/j.gca.2010.01.030

Seyfried, W. E., & Bischoff, J. L. (1979). Low temperature basalt alteration by sea water: An experimental study at 70°C and 150°C. *Geochimica et Cosmochimica Acta*, *43*(12), 1937–1947. https://doi.org/10.1016/0016-7037(79)90006-1

Sheppard, S. M. (1986). Characterization and isotopic variations in natural waters. In J. W. Valley, H. P. J. Taylor, & J. R. O'Neil (Eds.), *Stable isotopes in high temperature geological processes*, *Reviews in mineralogy and geochemistry* 16, 165–183.

Smith, D. L., Nuckels, E. I., Jones, R. L., & Cook, G. A. (1979). Distribution of heat flow and radioactive heat generation in northern Mexico. *Journal of Geophysical Research*, *84*(9), 2371–2379. https://doi.org/10.1029/jb084ib05p02371

Sonney, R., & Vuataz, F. D. (2008). Properties of geothermal fluids in Switzerland: A new interactive database. *Geothermics*, *37*(5), 496–509. https://doi.org/10.1016/j.geothermics.2008.07.001

Stober, I., & Bucher, K. (1999). Origin of salinity of deep groundwater in crystalline rocks. *Terra Nova*, *11*(4), 181–185. https://doi.org/10.1046/j.1365-3121.1999.00241.x

Stober, I., & Bucher, K. (2007). Hydraulic properties of the crystalline basement. *Hydrogeology Journal*, *15*(2), 213–224. https://doi.org/10.1007/s10040-006-0094-4

Stober, I., Giovanoli, F., Wiebe, V., & Bucher, K. (2022). Deep hydrochemical section through the Central Alps: Evolution of deep water in the continental upper crust and solute acquisition during water–rock-interaction along the Sedrun section of the Gotthard Base Tunnel. *Swiss Journal of Geosciences*, *115*(1), 9. https://doi.org/10.1186/s00015-022-00413-0

Stober, I., Zhong, J., Zhang, L., & Bucher, K. (2016). Deep hydrothermal fluid–rock interaction: The thermal springs of Da Qaidam, China. *Geofluids*, *16*(4), 711–728. https://doi.org/10.1111/gfl.12190

Storey, M., Rogers, G., Saunders, A. D., & Terrell, D. J. (1989). San Quintín volcanic field, Baja California, Mexico: "within-plate" magmatism following ridge subduction. *Terra Nova*, *1*(2), 195–202. https://doi.org/10.1111/j.1365-3121.1989.tb00352.x

Sutherland, R., Townend, J., Toy, V., Upton, P., Coussens, J., Allen, M., et al. (2017). Extreme hydrothermal conditions at an active plate-bounding fault. *Nature*, *546*(7656), 137–140. https://doi.org/10.1038/nature22355

Taillefer, A., Guillou-Frottier, L., Soliva, R., Magri, F., Lopez, S., Courrioux, G., et al. (2018). Topographic and faults control of hydrothermal circulation along dormant faults in an orogen. *Geochemistry, Geophysics, Geosystems*, *19*(12), 4972–4995. https://doi.org/10.1029/2018GC007965

Tian, J., Stefánsson, A., Li, Y., Li, L., Xing, L., Li, Z., et al. (2023). Geothermics Geochemistry of thermal fluids and the genesis of granite-hosted Huangshadong geothermal system. *Southeast China*, *109*, 1–12. https://doi.org/10.1016/j.geothermics.2023.102647

Torgersen, T. (1980). Controls on pore-fluid concentration of 4He and 222Rn and the calculation of 4He/222Rn ages. *Journal of Geochemical Exploration*, *13*(1), 57–75. https://doi.org/10.1016/0375-6742(80)90021-7

Tóth, J. (1962). A Theory of Groundwater Motion in Small Drainage Basins in Central Alberta, Canada. *Journal of Geophysical Research*, *67*(11), 4375–4388. https://doi.org/10.1029/jz067i011p04375

Tóth, J. (2009). *Gravitational systems of groundwater flow: Theory, evaluation, utilization*. Cambridge University Press.

Tsunogai, S. (1975). Sea salt particles transported to the land. *Tellus*, *27*(1), 51–58. https://doi.org/10.3402/tellusa.v27i1.9883

Upton, P., Craw, D., Yu, B., & Chen, Y. G. (2011). Controls on fluid flow in transpressive orogens, Taiwan and New Zealand. *Geological Society - Special Publications*, *359*(1), 249–265. https://doi.org/10.1144/SP359.14

Upton, P., Koons, P. O., & Chamberlain, C. P. (1995). Penetration of deformation-driven meteoric water into ductile rocks: Isotopic and model observations from the Southern Alps, New Zealand. *New Zealand Journal of Geology and Geophysics*, *38*(4), 535–543. https://doi.org/10.1080/00288306.1995.9514680

Vidal, F. V., Welhan, J., & Vidal, V. M. (1982). Stable isotopes of helium, nitrogen and carbon in a coastal submarine hydrothermal system. *Journal of Volcanology and Geothermal Research*, *12*(1–2), 101–110. https://doi.org/10.1016/0377-0273(82)90006-3

Vidal, V. M. V., Vidal, F. V., & Isaacs, J. D. (1981). Coastal submarine hydrothermal activity off northern Baja California: 2. Evolutionary history and isotope geochemistry. *Journal of Geophysical Research*, *86*(B10), 9451–9468. https://doi.org/10.1029/JB086iB10p09451

Waber, H. N., Schneeberger, R., Mäder, U. K., & Wanner, C. (2017). Constraints on Evolution and Residence time of Geothermal Water in Granitic Rocks at Grimsel (Switzerland). *Procedia Earth and Planetary Science*, *17*, 774–777. https://doi.org/10.1016/j.proeps.2017.01.026

Waber, H. N., & Smellie, J. A. T. (2008). Characterisation of pore water in crystalline rocks. *Applied Geochemistry*, *23*(7), 1834–1861. https://doi.org/10.1016/j.apgeochem.2008.02.007

Wanner, C., Bucher, K., Pogge von Strandmann, P. A. E., Waber, H. N., & Pettke, T. (2017). On the use of Li isotopes as a proxy for water–rock interaction in fractured crystalline rocks: A case study from the Gotthard rail base tunnel. *Geochimica et Cosmochimica Acta*, *198*, 396–418. https://doi.org/10.1016/j.gca.2016.11.003

Wanner, C., Diamond, L. W., & Alt-Epping, P. (2019). Quantification of 3-D thermal anomalies from surface observations of an orogenic geothermal system (Grimsel Pass, Swiss Alps). *Journal of Geophysical Research: Solid Earth*, *124*(11), 10839–10854. https://doi.org/10.1029/2019JB018335

Wanner, C., Peiffer, L., Sonnenthal, E., Spycher, N., Iovenitti, J., & Kennedy, B. M. (2014). Reactive transport modeling of the Dixie Valley geothermal area: Insights on flow and geothermometry. *Geothermics*, *51*, 130–141. https://doi.org/10.1016/j.geothermics.2013.12.003

Wanner, C., Waber, H. N., & Bucher, K. (2020). Geochemical evidence for regional and long-term topography-driven groundwater flow in an orogenic crystalline basement (Aar Massif, Switzerland). *Journal of Hydrology*, *581*, 124374. https://doi.org/10.1016/j.jhydrol.2019.124374

Weiss, R. F. (1971). Solubility of Helium and Neon in water and seawater. *Journal of Chemical and Engineering Data*, *16*(2), 235–241. https://doi.org/10.1021/je60049a019

Wetmore, P. H., Malservisi, R., Fletcher, J. M., Alsleben, H., Wilson, J., Callihan, S., et al. (2019). Slip history and the role of the Agua Blanca fault in the tectonics of the North American-Pacific plate boundary of southern California, USA and Baja California, Mexico. *Geosphere*, *15*(1), 119–145. https://doi.org/10.1130/GES01670.1

Whipp, D. M., & Ehlers, T. A. (2007). Influence of groundwater flow on thermochronometer-derived exhumation rates in the central Nepalese Himalaya. *Geology*, *35*(9), 851–854. https://doi.org/10.1130/G23788A.1

White, D. E., Brannock, W. W., & Murata, K. J. (1956). Silica in hot-spring waters. *Geochimica et Cosmochimica Acta*, *10*(1–2), 27–59. https://doi.org/10.1016/0016-7037(56)90010-2

Williams, A. E., & Rodoni, D. P. (1997). Regional isotope effects and application to hydrologic investigations in southwestern California. *Water Resources Research*, *33*(7), 1721–1729. https://doi.org/10.1029/97WR01035

Zijl, W. (1999). Scale aspects of groundwater flow and transport systems. *Hydrogeology Journal*, *7*(1), 139–150. https://doi.org/10.1007/s100400050185

Zúñiga, W. M. T. (2010). *Mountain block recharge in the Santo Tomás valley, Baja California, México*. Tesis de Maestría en Ciencias. Centro de Investigación Científica y de Educación Superior de Ensenada, Baja California.

Zuza, A. V., & Cao, W. (2020). Seismogenic thickness of California: Implications for thermal structure and seismic hazard. *Tectonophysics*, *782–783*. https://doi.org/10.1016/j.tecto.2020.228426